Journal of Wind Engineering & Industrial Aerodynamics 229 (2022) 105172

Contents lists available at ScienceDirect

Journal of Wind Engineering & Industrial Aerodynamics

journal homepage: www.elsevier.com/locate/jweia

Investigation of varying louver angles and positions on cross ventilation in a generic isolated building using CFD simulation

Vin Cent Tai [a,*], Joseph Wu Kai-Seun [b], Prasath Reuben Mathew [b], Lip Kean Moey [a], Xinwei Cheng [c], David Baglee [d]

[a] Centre for Modelling and Simulation, Faculty of Engineering, Built Environment & Information Technology, SEGi University, Selangor, Malaysia
[b] Faculty of Engineering, Built Environment & Information Technology, SEGi University, Selangor, Malaysia
[c] School of Mechanical and Aerospace Engineering, Queen's University Belfast, BT9 5AH, Belfast, United Kingdom
[d] School of Engineering, Faculty of Technology, University of Sunderland, SR1 3SD, Sunderland, United Kingdom

ARTICLE INFO

Keywords:
Natural cross ventilation
Louver angle
Isolated building
Air exchange efficiency
CFD

ABSTRACT

Louvers are an integral component of natural ventilation. This study presents a numerical analysis using computational fluid dynamics (CFD) on cross ventilation in an isolated building equipped with louvers. Opening configurations of (i) center-center, (ii) top-top, (iii) bottom-bottom, (iv) top-bottom and (v) bottom-top (whereby the configurations are defined as 'windward'-'leeward') with varying louver configurations of No-Louver (NL), 0°, 15°, 30° and 45° are studied. Atmospheric Boundary Layer (ABL) condition is applied at the inlet of the flow domain and Renormalization Group (RNG) k-ε turbulence model with enhanced wall function (EWT) is employed for the numerical simulations. Grid sensitivity analysis is performed using Grid Convergence Index (GCI) whilst model validation is performed using Factor of two of observation (FAC2) analysis. The highest dimensionless flow rate (DFR) is achieved by configuration top-top without louvers at 0.719. The highest air exchange efficiency (AEE) is obtained by louver angle of 15° for center-center configuration at 53.4%. The lowest AEE obtained is obtained at louver angle of 0° for top-top configuration at 20%, indicating short-circuiting of air. For configuration bottom-bottom with louver angle of 30°, high AEE is obtained but at the cost of reduced DFR. The optimal balance between AEE and DFR can be obtained by factor-optimization (α) as presented in this paper. The study concludes that opening position alongside louver angle plays an integral role on the internal airflow, pressure coefficient, DFR and AEE in natural cross ventilation.

1. Introduction

In Malaysia, the percentage of energy consumed by buildings alone is about 48% and this value is expected to increase as the country progresses further developmentally, transitioning from an agricultural-based economy to a technological and services-based economy (Hassan et al., 2014; Shaikh et al., 2017). In the United States, buildings consume the highest percentage of energy at 76% of the total electricity produced - out of which, 35% of the aforementioned value is used for Heating, Ventilation, & Air Conditioning (HVAC) systems (United States of America Department of Energy, 2015). This predicament has led to a particular focus on the reduction of excess energy usage in building HVAC systems (Green Building Council, 2000), of which includes the introduction of natural ventilation in buildings. Natural ventilation can be further enhanced by the application of louvers (Kosutova et al., 2019).

There are a plethora of variables that can affect the performance of louvers. The three main categories used to classify the variables are (i) environmental variables, (ii) louver geometry and (iii) output variables (Chandrashekaran, 2010; Aflaki et al., 2014; Elwan et al., 2018). Environmental variables represent the variables surrounding the geometry such as wind speed (and a subset of that, wind angles) as well as window to wall ratio. Louver geometry variables encompass factors such as coefficient of discharge (C_D), sizes of inlet and outlet, opening height and angle of louver. Output variables are the outcomes that are desired by the designer such as minimum air change per hour (ACH), internal air speed desired, pressure differentials at opening(s) and distribution of air at the reference plane.

The existing knowledge in the field of louvers in natural cross ventilation include the decreased volume flow rate through the building as the louver angle increases (Chandrashekaran, 2010). On top of that,

* Corresponding author.
E-mail address: taivincent@segi.edu.my (V.C. Tai).

https://doi.org/10.1016/j.jweia.2022.105172
Received 14 January 2022; Received in revised form 3 August 2022; Accepted 8 September 2022
Available online 18 September 2022

Nomenclature

A_o	Opening area [m^2]
A_E	Effective opening area [m^2]
C_D	Coefficient of discharge [-]
C_p	Pressure coefficient [-]
$C_{p,\ windward}$	Pressure coefficient at windward opening [-]
$C_{p,\ leeward}$	Pressure coefficient at leeward opening [-]
$C_{p,\ internal}$	Pressure coefficient at the internal of the building [-]
ΔC_p	Change in pressure coefficient between the windward and leeward opening [-]
H	Height of building [m]
I_u	Turbulence intensity at streamwise direction [m^2/s^2]
k	Turbulent kinetic energy [m^2/s^2]
k/U_{ref}^2	Dimensionless ratio of turbulent kinetic energy over the square of the reference velocity [-]
L	Length of building [m]
p	Formal order of accuracy [-]
r	Linear grid refinement factor [-]
Sct	Turbulent Schmidt number [-]
U^*_{ABL}	ABL friction velocity [m/s]
U	Streamwise velocity [m/s]
U_{ref}	Reference velocity [m/s]
U/U_{ref}	Dimensionless mean streamwise velocity ratio [-]
$\dot{V}$	Volume flow rate through the building [m^3/s]
W	Width of building [m]
Y_o	Aerodynamic roughness height [m]
Y_{ref}	Reference height [m]

Greek Letter

α	Factor-optimization [-]
ε	Turbulence dissipation rate [m2/s3]
ε_A	Air exchange efficiency [%]
ζ	Building wall thickness [mm]
κ	Von Karman constant [-]
$\overline{\tau}_r$	Residence time [s]
τ_{av}	Volume average age of air [s]
μ	Dynamic viscosity of air [Pa·s]
ω	Specific dissipation rate [1/s]

Abbreviations

ABL	Atmospheric Boundary Layer
ACH	Air Change per Hour [-]
AEE	Air Exchange Efficiency [%]
AOA	Age of Air [s]
BOI	Body of Influence
CFD	Computational Fluid Dynamics
DFR	Dimensionless Flow Rate
EWT	Enhanced Wall Treatment
FAC2	Factor of two of observation
FB	Fractional Bias
FS	Factor of Safety
GCI	Grid Convergence Index
NL	No-Louver
NMSE	Normalized Mean Square Error
PIV	Particle Image Velocimetry
RANS	Reynolds Averaged Navier-Stokes
RKE	Realizable k-ε
RNG	Renormalization Group
RSM	Reynolds Stress Model
SKE	Standard k-ε
SST	Shear Stress Transport
UDS	User Defined Scalar

when louvers are placed at the windward opening nearest to the roof, its volume flow rate is highest; but when louvers are placed at the windward opening nearest to the ground, its volume flow rate is lowest (Kosutova et al., 2019). Subsequently, an acceleration of flow is observed across the louver blades both at the windward and leeward openings (Kosutova et al., 2019).

When it comes to the knowledge gaps of louvers in natural cross ventilation, higher volume flow rate and air change per hour (ACH) is not associated with better mixing of air within the building. The variable that best tracks the mixing of air within a building is the air exchange efficiency (AEE). However, the study of AEE is not commonly performed attributed to the increased cell count demand required to obtain accurate AEE values.

This study aims: (i) to perform model validation with the numerical model by Kosutova et al. (2019), (ii) to investigate the impact of louver angle and opening position on the DFR through the building and (iii) to study the impact of louver angle and opening position on the age of air (AOA) and AEE within the building. This paper is organized as follows: Section 2 briefly presents the literature on the topic of natural ventilation. Section 3 explains the methodology for this paper. Section 4 provides the numerical results as well as the discussion of the results obtained, while Section 5 concludes the paper.

2. Related work

First and foremost, Tominaga and Blocken (2016) performed a numerical experiment and validated the results with a wind tunnel experiment to study the internal air pattern in a cross-flow building with openings for pollutant removal. The configurations investigated were, (i) up-up, (ii) up-down, (iii) down-down, (iv) down-up and (v) mid-mid (whereby the configurations are defined by 'windward'-'leeward'). The authors concluded that the (v) mid-mid configuration was most effective in ventilation of pollutants, due to higher efficiency of the entrainment process by the flapping jet characterized by a district Kelvin-Hemlholtz instability which leads to formation and shedding discrete vortical structures. On the other hand, configurations (i) up-up and (ii) up-down were restricted by the ceiling, meanwhile configurations (iii) down-down and (iv) down-up were restricted by the floor. The work showed that inlet opening position has strong influence on flapping jet behavior and Kevin-Helmholtz instability which govern the entrainment process, while the influence of the outlet opening position is rather limited.

Meanwhile, Kosutova et al. (2019) studied the louver location in a cross-flow configuration to determine the optimum configuration for air mixing within a room for a generic isolated building. Windward and leeward heights were manipulated while maintaining a louver angle of 15°. These configurations included, (i) up-up, (ii) mid-mid, (iii) down-down and (iv) up-down. The CFD results were compared to the experimental data collected using Particle Image Velocimetry (PIV). Reynolds-Averaged Navier-Stokes (RANS) turbulence models of Renormalization Group (RNG), Shear Stress Transport (SST) and Reynolds Stress Model (RSM) were used for the CFD studies. The study showed that RSM turbulence model gave the closest values to the experimental data. Louvers reduced the volume flow rate because of the decrease in effective area as compared to that of openings without louvers. However, configurations with louvers provided a better AEE, thus indicating that the mixture of air within the building is better among configurations with louvers present. The highest AEE at 45% was obtained by the center-center configuration in the presence of louvers because the incoming jet was directed upwards thereby encouraging

mixing to occur within the building.

Moving on, Chandrashekaran (2010) studied the performance of various louver angles at different velocities of 2.9, 4.5 and 6.1 m/s using a wind tunnel experiment. The numerical solution using RANS Standard k-ε (SKE) was validated with the experimental results. At louver angles of 0°, 15° and 30° there was an acceleration through the center section of the windward louver. Subsequently, at louver angle of 45°, an overall reduction in internal flow velocity was observed. Thus, the author proposed the usage of 45° louver angles when external air velocities are high. The reduction of flow velocity that occurred was due to the decrease in the effective opening area. The higher resistance present in higher louver angles caused turbulence to occur inside the room which enabled better mixing of air. This was also mentioned by Kosutova et al. (2019). Moreover, the 45° louver angle showed an increase in air mixing within the room at the upper area instead of the region near the worktable, thus the author concludes that such a configuration is suitable for schools and living rooms. Such has also been remarked by Kouhirostami (2020). On top of that, reduced air mixing at the lower region of the room prevents wind chill factor.

Recent papers by Zheng et al. (2020) studied the effects of shading louvers on natural ventilation with varying angles. The performance of non-shaded louvers and shaded louvers of 0°, 15°, 30°, 45°, 60° and 75° at velocity 3.41 m/s were studied. Using the coupled airflow model, the authors discovered that the shaded louver angle of 0° had a higher ventilation rate of 284 m^3/h than the model without such shading louvers at 276 m^3/h. This could be due to the presence of the shading

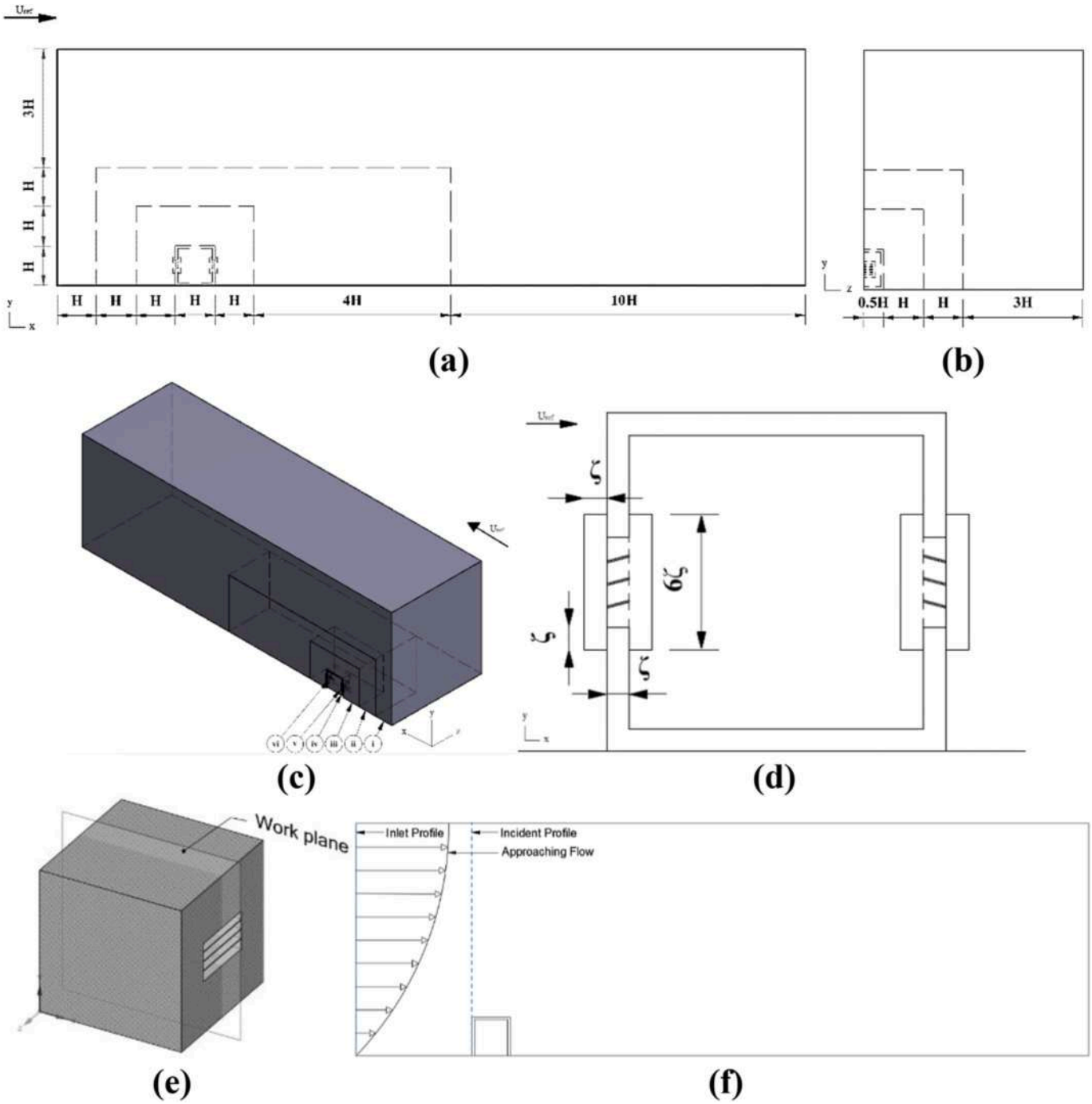

Fig. 1. Computational domain (a) Front view (b) Side view (c) Isometric view (d) Windward-Leeward BOI (e) Work plane and (f) Inlet and Incident profile.

louvers which diverted the windward airflow. Although louver angles were changed, however the locations of the opening positions were not manipulated. CFD studies were conducted with RANS models of SKE, Realizable k-ε (RKE), RNG, SST and RSM. The authors concluded that RKE and SST had the best performance when compared with the experimental results. The author concluded that the simplified engineering model which uses the pressure coefficient at the windward and leeward openings, fails to quantify the volume flow rate of louvers in natural cross ventilation thus producing a large deviation.

The study of the performance of louvers in natural ventilation is limited to a few published papers. To the best knowledge of the authors, from the earliest paper written with regards to the implementation of louvers to the time of writing, there has not been any published work that manipulates the opening positions and angle of louvers concurrently. The study of the placement of varying louver positions and angles is imperative because of the different internal air profiles, internal velocities, pressure coefficient, AOA, DFR and AEE produced. The novelty presented by this paper includes the variable AOA and AEE for louvers in different angles and opening locations.

3. Methodology

3.1. Model geometry, computational domain, and building configuration

The building is designed with dimensions of 150 mm × 150 mm x 150 mm (L x W x H). The flow domain is designed with specification, 3H distance from the front of the building model to the inlet to prevent unintended streamwise gradients in the approaching flow profiles (Kosutova et al., 2019; Ramponi and Blocken, 2012), 5H from the sides of the building to the side and to the top wall of the flow domain, and 15H from the back of the building to the outlet – whereby H represents the height of the building, of which in this case is 0.15 m. The computational domain blockage ratio is less than 3%. The dimensions of the flow domain are in line with the best practices as reported in the literature (Kosutova et al., 2019; Ramponi and Blocken, 2012; Perén et al., 2015).

The front view of the computational domain can be seen in Fig. 1(a), meanwhile its side view can be seen in Fig. 1(b). The isometric view can be observed in Fig. 1(c). Fig. 1(c)(i) is the flow domain, 1(c)(ii) is the Far BOI, 1(c)(iii) is the Near BOI, 1(c)(iv) is the House BOI, 1(c)(v) is the Windward BOI and 1(c)(vi) is the Leeward BOI. Fig. 1(e) shows the work plane that intersects the geometry at the middle, while the inlet and incident profile are shown in Fig. 1(f).

In Fig. 1(d), the dimensions for the Windward BOI and Leeward BOI are shown. These BOIs are designed according to the thickness of the building, ζ. In this numerical simulation, ζ equals 10 mm.

In this paper, five different opening positions are considered: (i) center-center, (ii) top-top, (iii) bottom-bottom, (iv) top-bottom and (v) bottom-top where the dimensions are shown in Fig. 2. The dimensions of the openings are 70 mm × 40 mm (W x H) with a depth of 10 mm. Additionally, a basic configuration with no louvers (i) No-Louver (NL) alongside four louver angles are considered, (ii) 0°, (iii) 15°, (iv) 30° and (v) 45° as shown in Fig. 3. This amounts to a total of 25 numerical cases as shown in Table 1 below. The meshing and CFD simulations are conducted using ANSYS 2020 R1. The dynamic viscosity of air, μ is set to 1.79×10^{-5} Pa·s. Volume mesh refinement regions known as body of influences (BOIs) have been used to locally adopt the mesh in the desired zones as shown in Fig. 4(a) (van Hooff and Blocken, 2010; Moey et al., 2021a; Sofotasiou et al., 2017; Krishna et al., 2019). The Near BOI has a 150 mm offset distance from the top and the side walls of the building, as shown in Fig. 1(c)(iii). The second and third BOI named Windward BOI and Leeward BOI are placed at the windward and leeward openings to accurately capture the flow through the louvers as shown in Fig. 1(c)(v) and (vi) respectively. The fourth BOI named Far BOI is placed to capture the approaching flow and the separation flow outside the building as shown in Fig. 1(c)(ii). A fifth BOI named House BOI encloses the building itself as observed in Fig. 1(c)(iv).

Poly-hexcore cells are used in the meshing as shown in Fig. 4(a). 20 prism layers with 1.2 growth rate are applied to the ground, building and its louvers, as shown in Fig. 4(b). The first cell height at the building is 35 μm and its corresponding Y+ is found to be less than 0.60. The skewness of the mesh for all numerical cases is controlled not to exceed 0.65. Fine element sizes were applied to the model edges to yield the desired mesh quality and to control the maximum Y+ values. The final mesh created has a maximum Y+ value of 1.5 for the walls and louvers, meanwhile the mesh size for the ground is less than 0.035m and its maximum Y+ is 2.1. The corresponding average values of Y+ for walls, louvers, and ground are 0.5742, 0.5149, and 1.5087, respectively.

3.2. Atmospheric boundary layer (ABL)

An ABL file is interpreted to create the desired velocity profile from the inlet. The ABL friction velocity, U^*_{ABL} is calculated using Equation (1) with a reference velocity, U_{ref} of 1.9 m/s and a reference height, Y_{ref} of 0.15 m. Additionally, the Von Karman constant, κ of 0.4 with an aerodynamic roughness height, Y_0 of 0.0024 m are used.

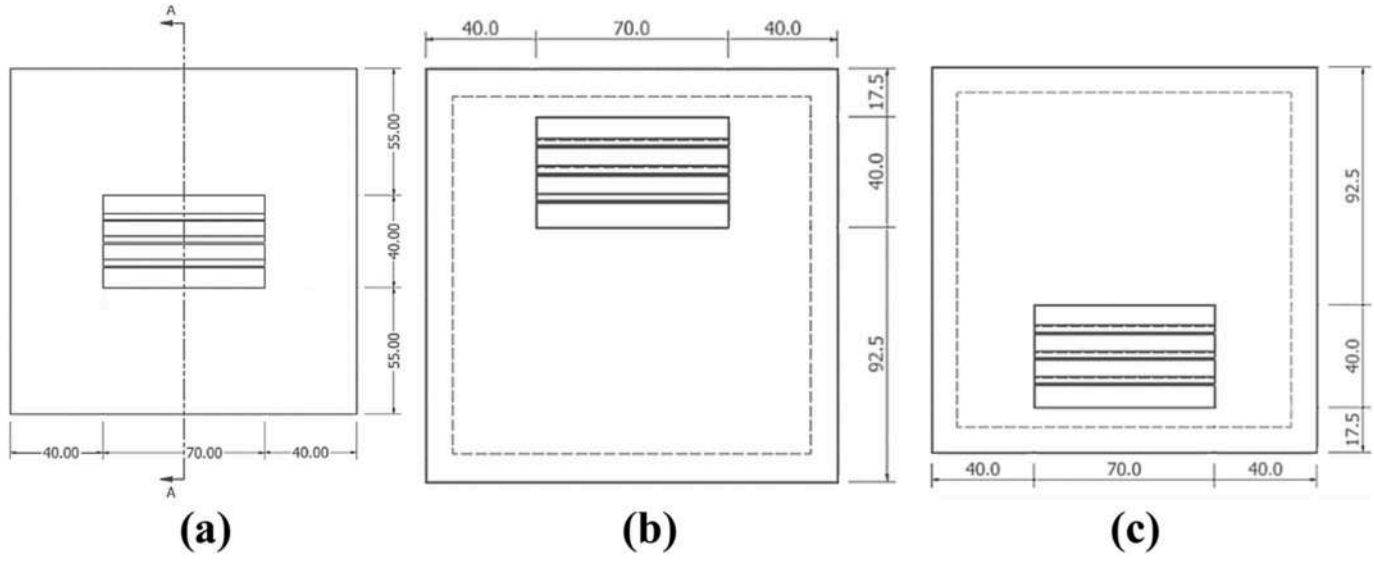

Fig. 2. Building opening dimensions at (a) center (b) top and (c) bottom.

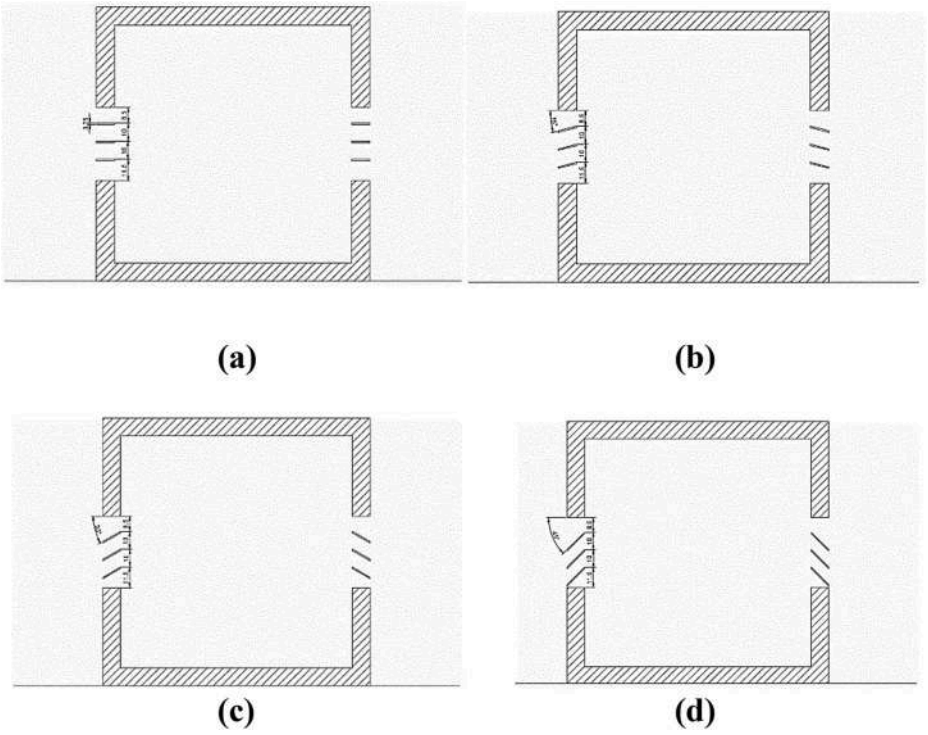

Fig. 3. Section A-A for varying louver angles of (a) 0° (b) 15° (c) 30° and (d) 45°.

Table 1
Simulation cases.

Case	Opening Location	Louver Angle
1	Center-Center	No-Louver (NL)
2		0°
3		15°
4		30°
5		45°
6	Top-Top	No-Louver (NL)
7		0°
8		15°
9		30°
10		45°
11	Bottom-Bottom	No-Louver (NL)
12		0°
13		15°
14		30°
15		45°
16	Top-Bottom	No-Louver (NL)
17		0°
18		15°
19		30°
20		45°
21	Bottom-Top	No-Louver (NL)
22		0°
23		15°
24		30°
25		45°

$$U^*_{ABL} = \frac{U_{ref} \times \kappa}{\log\left(\frac{Y_{ref}+Y_0}{Y_0}\right)} \tag{1}$$

The inlet velocity profile is obtained using the ABL friction velocity, U^*_{ABL} as shown in Equation (2) while the turbulence dissipation rate, ε is calculated from Equation (3). The turbulence intensity in streamwise direction, I_u is found to be 10% at building height of 0.15 m (Kosutova et al., 2019).

$$U = \frac{U^*_{ABL}}{\kappa}\log\left(\frac{Y_{ref}+Y_0}{Y_0}\right) \tag{2}$$

$$\varepsilon = \frac{\left(U^*_{ABL}\right)^3}{\kappa\left(Y_{ref}+Y_0\right)} \tag{3}$$

For the flow domain, zero specific shear stress is specified for the top and side walls. The outlet is set as pressure-outlet, no-slip boundary condition is applied to the building walls and ground, and symmetry is applied at the vertical centre plane along the wind direction. The inlet is set as velocity-inlet with values of velocity magnitude, turbulent kinetic energy, and turbulence dissipation rate generated by the ABL file. The turbulence intensity in streamwise direction (I_u) is obtained by Equation (4)

$$I_u = \frac{\sigma_u}{U_{ref}} \tag{4}$$

The turbulent kinetic energy profile, k is obtained by obtaining the standard deviation of the turbulent fluctuations in three dimensions as shown in Equation (5).

$$k = \frac{1}{2}\cdot\left(\sigma_u^2+\sigma_v^2+\sigma_w^2\right) \tag{5}$$

Then, since only turbulent fluctuations of σ_u^2 and σ_v^2 were measured in the wind tunnel by Kosutova et al. (2019), and then by assuming $\sigma_u^2 \approx \sigma_v^2+\sigma_w^2$ (Ramponi and Blocken, 2012), thus Equation (6) can be obtained.

$$k = \frac{1}{2}\cdot\left[\sigma_u^2+\sigma_v^2+\left(\sigma_u^2-\sigma_v^2\right)\right] = \sigma_u^2 \tag{6}$$

The comparison of turbulence intensity in streamwise direction (I_u) of Kosutova et al. (2019)'s model and Grid B showing good agreement is shown in Fig. 5(c). In the wind tunnel, a series of obstacles were added upstream of the building to create a neutral atmospheric boundary layer (ABL) approach flow. The comparison between the inlet velocity profile and the incident velocity profile for Kosutova et al. (2019)'s model and

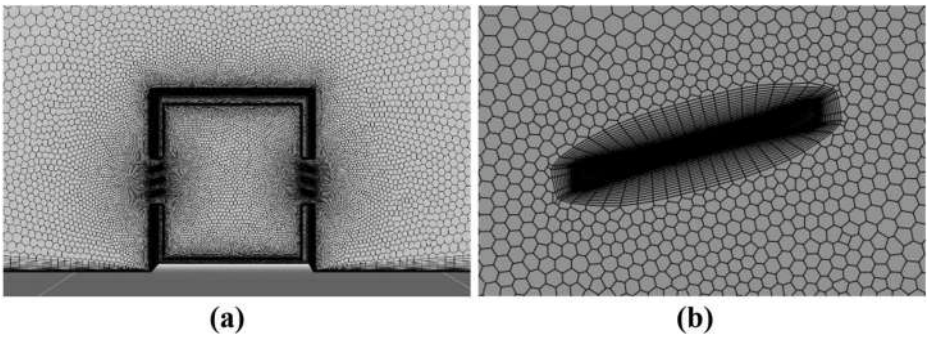

Fig. 4. (a) Poly-hexcore mesh surrounding the house and (b) Prism layer around the louver.

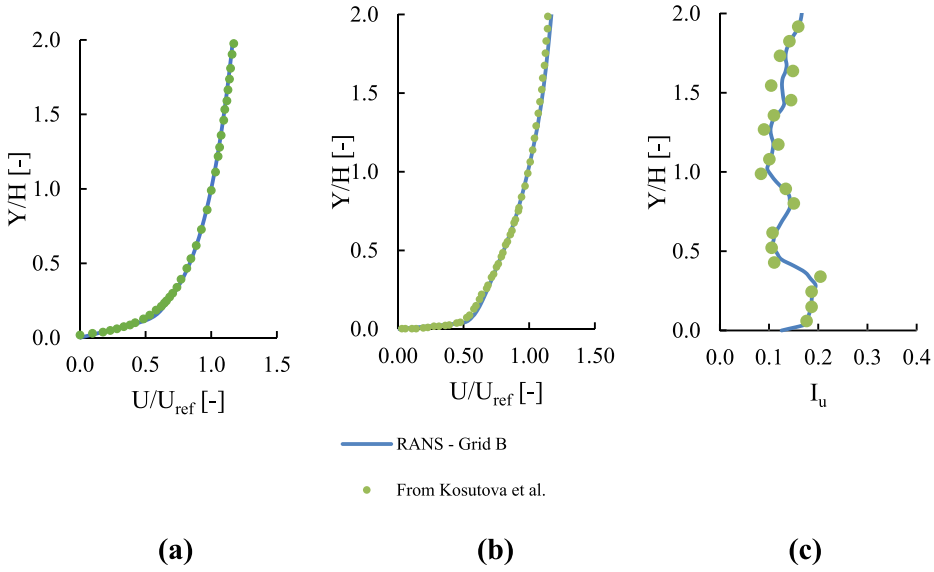

Fig. 5. Velocity profiles of Kosutova et al. (Kosutova et al., 2019) and Grid B compared at (a) Inlet Profile and (b) Incident profile. The turbulence intensity in streamwise direction, (I_u) of Kosutova et al. (Kosutova et al., 2019) compared at (c) Inlet Profile.

Grid B are shown in Fig. 5(a) and (b) respectively. Grid B is selected based on the analysis performed in the following section. The comparison shows good agreement between the inlet and incident velocity profiles.

3.3. Fluent solver settings

All the CFD simulations are conducted using ANSYS 2020 R1. RNG turbulence model from the 3D steady RANS is employed. Enhanced wall treatment (EWT) is applied to all surfaces to resolve the viscous sublayer, as EWT showed good performance in studying velocity profiles but with a longer computational time trade-off (El Gharbi et al., 2009). SIMPLE scheme is used for pressure-velocity coupling, while Least Squares Cell-Based gradient is chosen for spatial discretization (Moey et al., 2021a). Second-order interpolation scheme is chosen for pressure, while second-order upwind discretization schemes are selected for momentum, turbulent kinetic energy, turbulence dissipation rate, and User Defined Scalar (UDS) to yield more accurate results (van Hooff et al., 2017). Hybrid initialization is used in this numerical simulation. The convergence criteria are set to 1×10^{-4} for continuity and 1×10^{-5} for x, y, z-velocities, k, ε and UDS residuals (Kosutova et al., 2019). All solutions converged after approximately 3000 iterations.

3.4. Grid sensitivity analysis

The number of cells used for all 25 cases is 3,232,464, also known as the reference grid. The reference grid is determined through grid sensitivity analysis via the Grid Convergence Index (GCI) as shown in Equation (7) (Kosutova et al., 2019; Ramponi and Blocken, 2012; van Hooff et al., 2017; Gilani et al., 2013). The factor of safety (SF) when considering 3 or more grids is 1.25 (Wilcox, 2006). The linear grid refinement factor, r is $\sqrt{2}$ while the formal order of accuracy, p is 2 because second-order discretization scheme is used. Grid B is obtained by dividing the global and local scope sizing by $\sqrt{2}$, and similarly Grid C is obtained by further refining the global and local scope sizing by $\sqrt{2}$.

$$GCI = SF\left|\frac{r^p \frac{U_{coarse} - U_{fine}}{U_{ref}}}{r^p - 1}\right| \tag{7}$$

The cell counts for Grids A, B, and C are 1,953,517, 3,232,464 and 5,868,167, respectively. Fig. 6 shows the grid sensitivity analysis performed. At X/H = 0.2, the GCI value for Grid A is 4.72%, and 0.73% for Grid B. For X/H = 0.4, the GCI values are 4.62% for Grid A and 0.90% for Grid B. At location X/H = 0.6 the GCI values for Grids A and B are 4.20% and 0.97%, respectively. At location X/H = 0.8, the GCI values are 4.21% for Grid A and 1.68% for Grid B. Therefore, there is a trend observed where the grids have a reduced GCI as the grids become finer. The mean GCI for Grid A and Grid B across all 4 locations is 4.44% and 1.07% respectively. Grid B is selected as the reference grid for this study because its GCI value is close to 1%. Fig. 6 shows the grid sensitivity analysis showing good agreement.

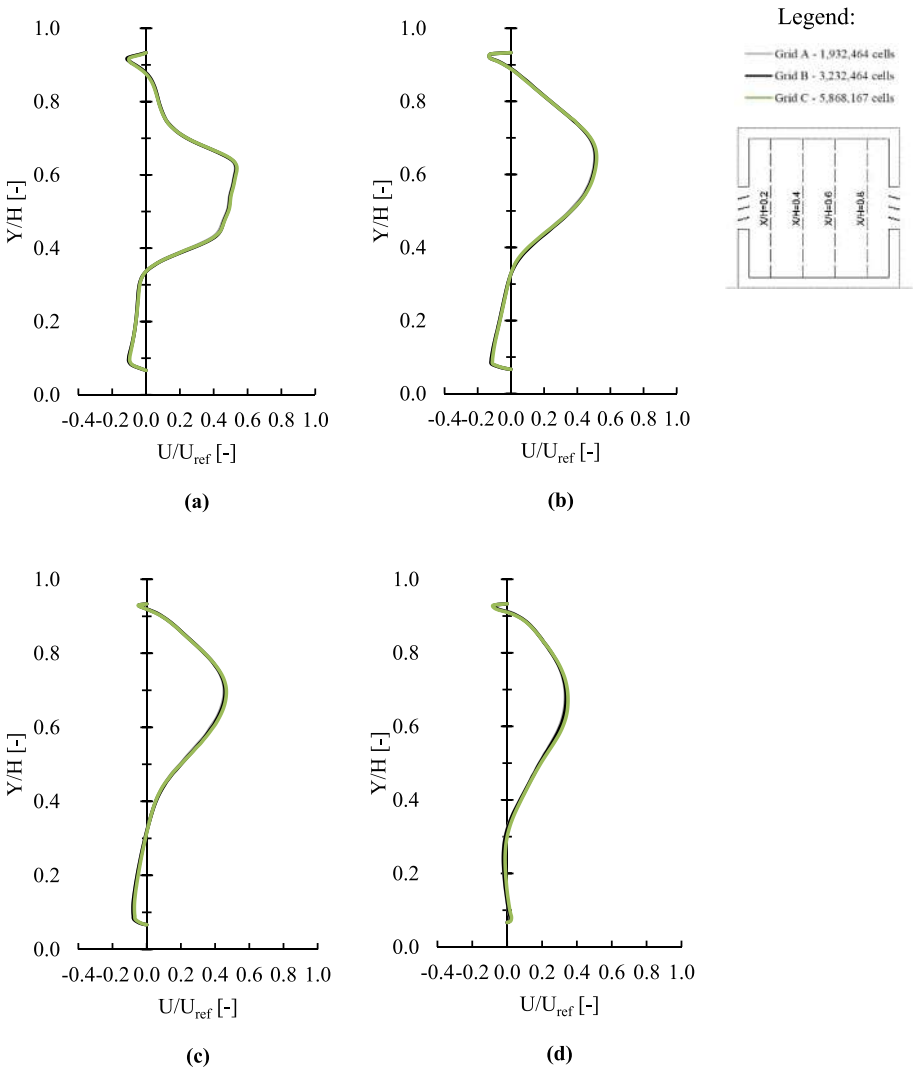

Fig. 6. Grid sensitivity analysis for (a) X/H = 0.2 (b) X/H = 0.4 (c) X/H = 0.6 and (d) X/H = 0.8.

3.5. Model verification

The quantitative metrics used for model verification are the Factor of two of observation (FAC2) which was first proposed by Schatzmann et al. (2010) and Root Mean Square Error (RMSE). FAC2 is chosen in this study because it is a robust model validation method for CFD with regards to the occurrence of sporadic occurring high or low observations and predictions (Schatzmann et al., 2010) and it is adopted by many authors (Kosutova et al., 2019; van Hooff et al., 2017; Shirzadi et al., 2020). FAC2 is obtained using Equation (8).

$$FAC2 = \frac{1}{n}\sum_{i=1}^{n} N_i$$

where,

$$N_i = \begin{cases} 1 & \text{if } 0.5 \le \dfrac{P_i}{O_i} \le 2 \\ 0; & \text{otherwise} \end{cases} \tag{8}$$

whereby, P_i is the value of the velocity profile obtained from the reference grid, meanwhile O_i is the value obtained from the RNG k-ε results published by Kosutova et al. (2019). When the observed value is below the compared value, but within the lower limit threshold, then it is acceptable; similarly, when it is above the compared value, but within the higher limit threshold, then it is also acceptable. For an ideal set of data, the FAC2 is 1. In the model verification with Kosutova et al. (2019), for location X/H = 0.2 the FAC2 is 0.88, ergo 88% of the data falls within the acceptable range of error. For X/H = 0.4, 0.6 and 0.8, their respective FAC2 values are 0.81, 0.86 and 0.82. The average of the obtained FAC2 values is 0.843. This is considered acceptable.

The other validation metric used in this study, RMSE is obtained using the following equation:

$$RMSE = \sqrt{\frac{1}{n}\sum_{i=1}^{n}(P_i - Q_i)^2} \tag{9}$$

where, Q_i is the experimental velocity profile published by Kosutova et al. (2019). The RMSE values obtained with Grid B are 6.411%, 4.863%, 6.582%, and 6.706% for X/H = 0.2, 0.4, 0.6, and 0.8, respectively. The RMSE values obtained using Equation (9) for the RNG k-ε results published by Kosutova et al. (2019) are 7.386%, 5.506%, 4.904%, and 5.426% for X/H = 0.2, 0.4, 0.6, and 0.8, respectively. All RMSE values obtained with Grid B are within the maximum RMSE value of the RNG k-ε model by Kosutova et al. (2019). Fig. 7(a), (b), 7(c) and 7 (d) show the comparison of the reference grid which is Grid B with 3, 232,464 cells against Kosutova et al. (2019)'s RNG k-ε model and the wind tunnel PIV values showing good agreement.

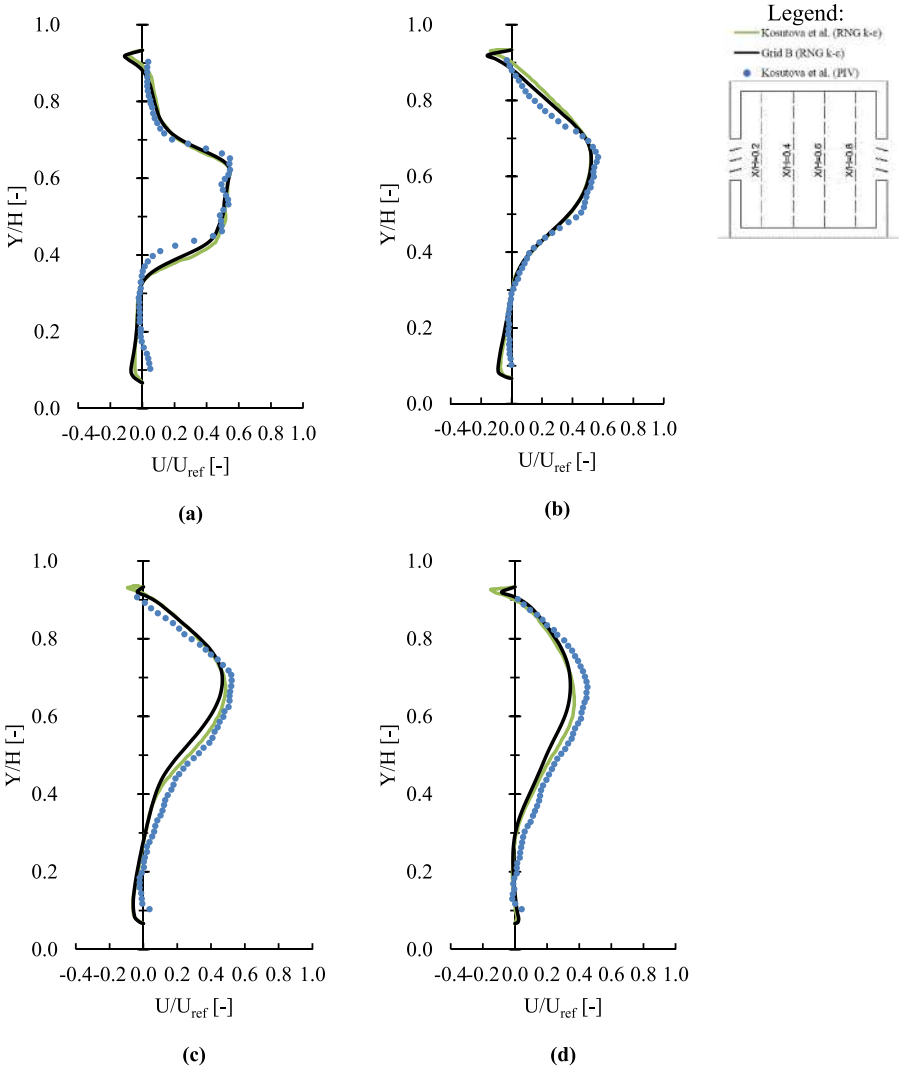

Fig. 7. Model validation of the reference grid with Kosutova et al. (Kosutova et al., 2019)'s PIV and RNG k-ε for locations (a) X/H = 0.2 (b) X/H = 0.4 (c) X/H = 0.6 and (d) X/H = 0.8.

4. Simulation results

The variable of study is the mean streamwise velocity ratio, U/U_{ref}. It is obtained by dividing the velocity at the region of study with the reference velocity, U_{ref} of 1.9 m/s. Referring to the velocity profile of center-center configuration shown in Fig. 8, as the louver angle increases from NL to 45°, the maximum U/U_{ref} recorded decreases. The effect of the jet produced after the air flowed through the opening is shown at the peak velocity in the velocity profile. The decrease in the recorded maximum U/U_{ref} is expected since the increase in louver angle causes a reduction in flow velocity because of the reduction in the effective opening area. As the louver angle increases, so does the height of the peak velocity as anticipated given that the jet is angled higher due to the louvers. At locations X/H = 0.6 and 0.8, comparing NL and 0°, the latter shows the peak velocity remains meanwhile the former shows the jet drifting downwards toward the floor. At locations X/H = 0.4, 0.6 and 0.8, louver angles of 30° and 45° share relatively similar velocity profiles.

Velocity profiles for top-top configuration are presented in Fig. 9. Louver angles of 30° and 45° show similar velocity profiles at X/H = 0.2, 0.4, 0.6 and 0.8 at regions of low velocities in the range of $0 \leq Y/H \leq 0.6$. Furthermore, top-top configuration produces similar peak velocities at the region of $0.8 \leq Y/H \leq 0.9$ because the jet produced by the louvers is driven against the ceiling and thus preventing the jet from spreading (Kosutova et al., 2019).

The velocity profile for bottom-bottom configuration is shown in Fig. 10. Similar to the center-center configuration, when the louver angle increases from 0° to 45°, the maximum U/U_{ref} decreases. As the louver angle increases, so does the height of the peak velocity since the jet is angled higher. High velocity is observed at the bottom region as predicted since the opening of the geometry is at the bottom region. At X/H = 0.8, louver angles of 30° and 45° show similar velocity profiles.

Fig. 11 shows the velocity profile for the top-bottom configuration. Louver angles of 30° and 45° show similar velocity profiles at region $0.8 \leq Y/H \leq 0.9$. The jet from the windward opening is angled toward the ceiling preventing the jet from spreading, similar to the phenomenon observed at top-top configuration.

Fig. 12 shows the velocity profiles for bottom-top configuration. As observed in center-center and bottom-bottom configurations, as the louver angle increases, so does the height of the peak velocity because the jet is angled higher. At X/H = 0.6 and 0.8, louver angles of 30° and 45° display similar velocity profiles. This means, the magnitude of the internal flow is relatively similar in these regions.

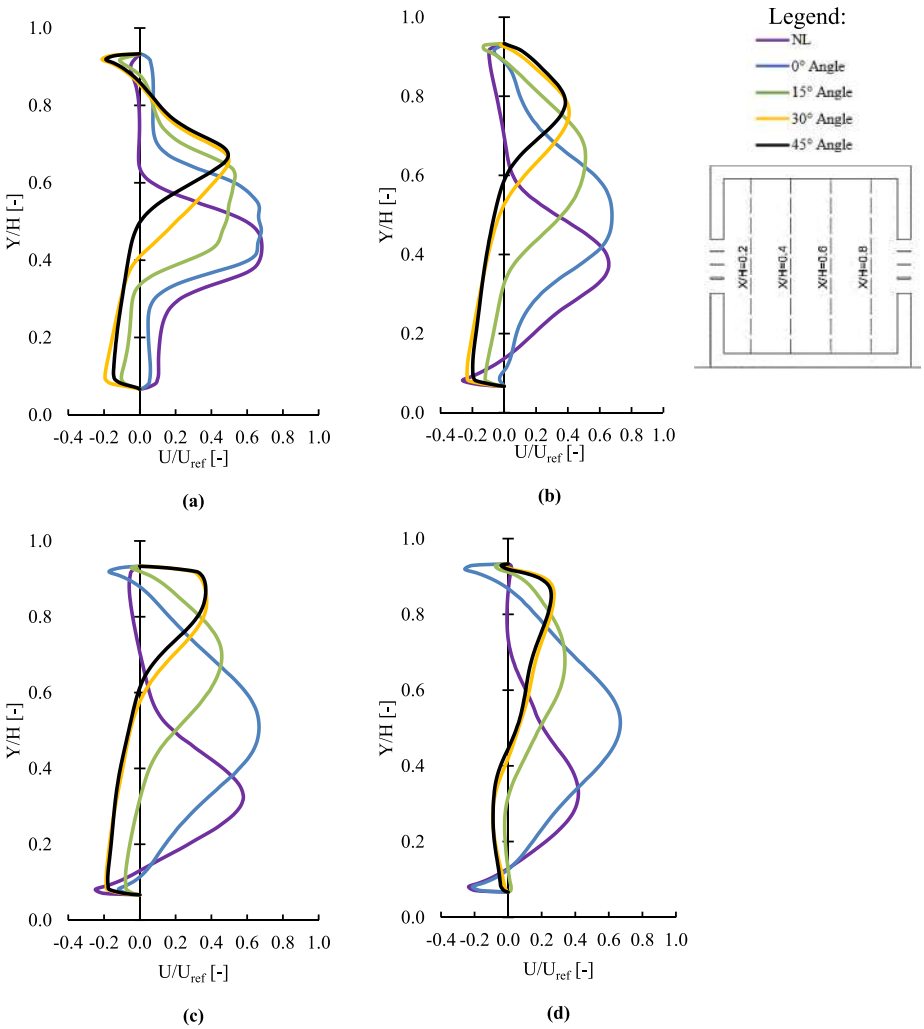

Fig. 8. Y/H against U/U_{ref} for louver angles of 0°, 15°, 30° and 45° for center-center configuration at (a) X/H = 0.2, (b) X/H = 0.4, (c) X/H = 0.6 and (d) X/H = 0.8.

4.1. Dimensionless U/U_{ref}

Dimensionless U/U_{ref} is obtained by dividing the mean streamwise velocity, U with the reference velocity, U_{ref} of 1.9 m/s. Dimensionless U/U_{ref} contours are shown in Table 2. Referring to Table 2, for the louvers located at the windward and leeward region, there is a sudden increase in velocity observed. This occurs for all louver angles for all the configurations studied. By observing the contours, an acceleration of velocity is seen at the regions between the louver blades up to a factor of 1.1 times the reference velocity. This sudden acceleration phenomenon is most prominent for top-top configuration.

The deflection of the upward jet is less pronounced as the louver angle increases. As for the jet produced by the flow exiting the louver at the windward location, one can observe a decreasing jet flow as the louver angle increases from 0° to 45°. A horseshoe-shaped vortex is present at the bottom region of the windward wall as shown in Table 5. This recirculation region is attributed to the incoming flow at the windward wall, as reported by several studies (Moey et al., 2018; Meroney, 2009). Subsequently, for configurations where the windward opening is located at the top e.g. top-top and top-bottom, the jet is directed to the ceiling and proceeds to attach to the ceiling attributed to the Coanda effect (Tominaga and Blocken, 2016).

By comparing the configurations NL and 0°, one can observe the NL configuration having a downward trajectory after passing through the windward opening. Meanwhile, in the presence of 0° louvers, the jet has a relatively straight trajectory after passing through the windward opening. This is most noticeable at configurations center-center, bottom-bottom and bottom-top. The presence of 0° louvers at the top-top configuration is seen to reduce the Coanda effect.

For louver angles of 15°, 30° and 45°, an upward jet deflection is observed after passing through the windward louvers. Such phenomenon has been reported by Kosutova et al. (2019). As the louver angle increases, so does the angle of the upward jet deflection.

For configuration down-down in the presence of 15°, 30° and 45° louvers, the jet is deflected upwards and then proceeds to flow downwards since the leeward louver opening is located at the bottom. Meanwhile, the velocity at the region near the windward opening decreases as the louver angle increases, similar to that obtained by Chandrashekaran (2010).

4.2. Pressure coefficient, C_p

$$C_p = \frac{P - P_s}{\frac{1}{2}\rho U_{ref}^2} \tag{10}$$

$$\Delta C_p = C_{p,\ windward} - C_{p,\ leeward} \tag{11}$$

Pressure coefficient, C_p is a non-dimensional ratio of the static pressure of a particular region over the free stream static pressure as shown in Equation (10). By taking the pressure coefficient at the exterior surface of the windward opening, $C_{p,\ windward}$ and subtracting it with the pressure coefficient at the exterior surface of the leeward opening, $C_{p,}$

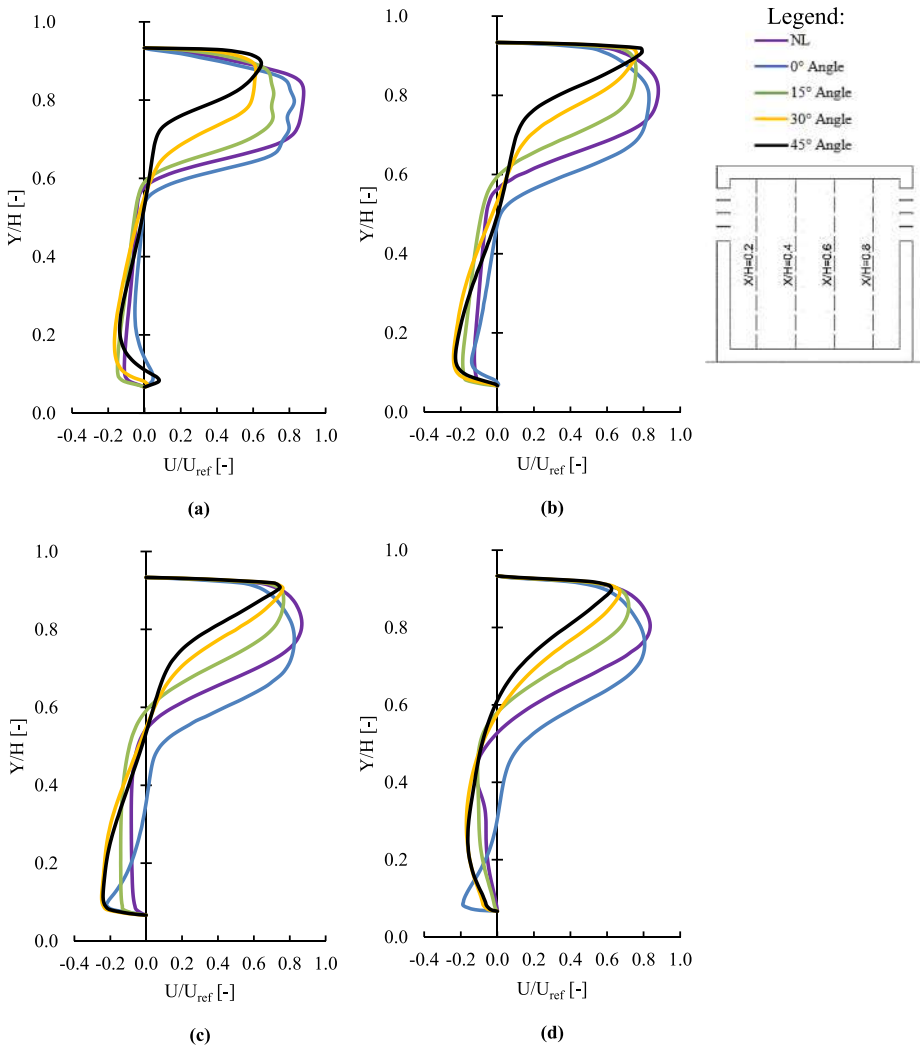

Fig. 9. Y/H against U/U_{ref} for louver angles of 0°, 15°, 30° and 45° for top-top configuration at (a) X/H = 0.2, (b) X/H = 0.4, (c) X/H = 0.6 and (d) X/H = 0.8.

leeward, the change in pressure coefficient between the windward and leeward opening can be obtained, denoted as ΔC_p as shown in Equation (11).

The pressure coefficient, C_p contours are shown in Table 3. A stagnation pressure region is observed at the top edge of the windward wall. The flow separates around the top, the sides, and the front of the building. This flow then proceeds to reattach, resulting in a negative C_p at the top of the model. The $C_{p,\ windward}$ and $C_{p,\ leeward}$ changes for different louver angles and opening positions. This thus causes the internal pressure coefficient, $C_{p,\ internal}$ to change and is observed in the contours by the different C_p values in the interior of the geometry. At the leeward opening, the $C_{p,\ leeward}$ has a negative value which is similar to that which was obtained by Chandrashekaran (2010).

It is pertinent to note that, the $C_{p,\ windward}$ at configuration top-top did not have the same $C_{p,\ windward}$ for configuration top-bottom despite both configurations having windward openings at the top. Similarly, $C_{p,\ windward}$ at configuration bottom-bottom which did not have similar $C_{p,\ windward}$ as the configuration bottom-top despite both configurations having similar openings at the windward bottom. The same is also observed for the pressure coefficient at the leeward wall, $C_{p,\ leeward}$. Therefore, the pressure coefficient at the windward opening is dependent on the position of the leeward opening; likewise, the pressure coefficient at the leeward opening is dependent on the position of the windward opening. As the louver angle increases from 0° to 45°, there is an increase in the ΔC_p as shown in Fig. 13.

4.3. Dimensionless k/U_{ref}^2

For the k/U_{ref}^2 contours reported in Table 4, high k/U_{ref}^2 is observed at the windward opening for all cases which is expected to occur since air flows from the inlet to the windward wall and no obstacles are surrounding the house (Shirzadi et al., 2021). On top of that, high k/U_{ref}^2 has also been observed at the leeward openings. High k/U_{ref}^2 is seen at the roof of the building due to the flow separation occurring in that region for all cases (Kosutova et al., 2019; Shirzadi et al., 2021). For center-center, the k/U_{ref}^2 at the leeward opening decreases from 0.02 to 0.01 as the louver angle increases from 0° to 45°, respectively. The same phenomenon of decreasing k/U_{ref}^2 is observed for top-top and bottom-bottom openings. However, this phenomenon is not observed for top-bottom and bottom-top.

In the interior of the model for top-bottom configuration, high k/U_{ref}^2 is observed at the leeward opening attributed to the flow being forced to flow downward to exit the building. This is observed for all top-bottom opening configurations NL, 0°, 15°, 30° and 45°.

For top-bottom configurations, at the top right of the internal building, there is a recirculation region. The recirculation region is evident in the streamline contour as shown in Table 5. The presence of the recirculation vortex is confirmed as k/U_{ref}^2 at that region is 0.02. The effect of recirculation vortex, although miniscule, has effects on the k/U_{ref}^2.

At the leeward openings, the highest values of k/U_{ref}^2 of 0.05 are

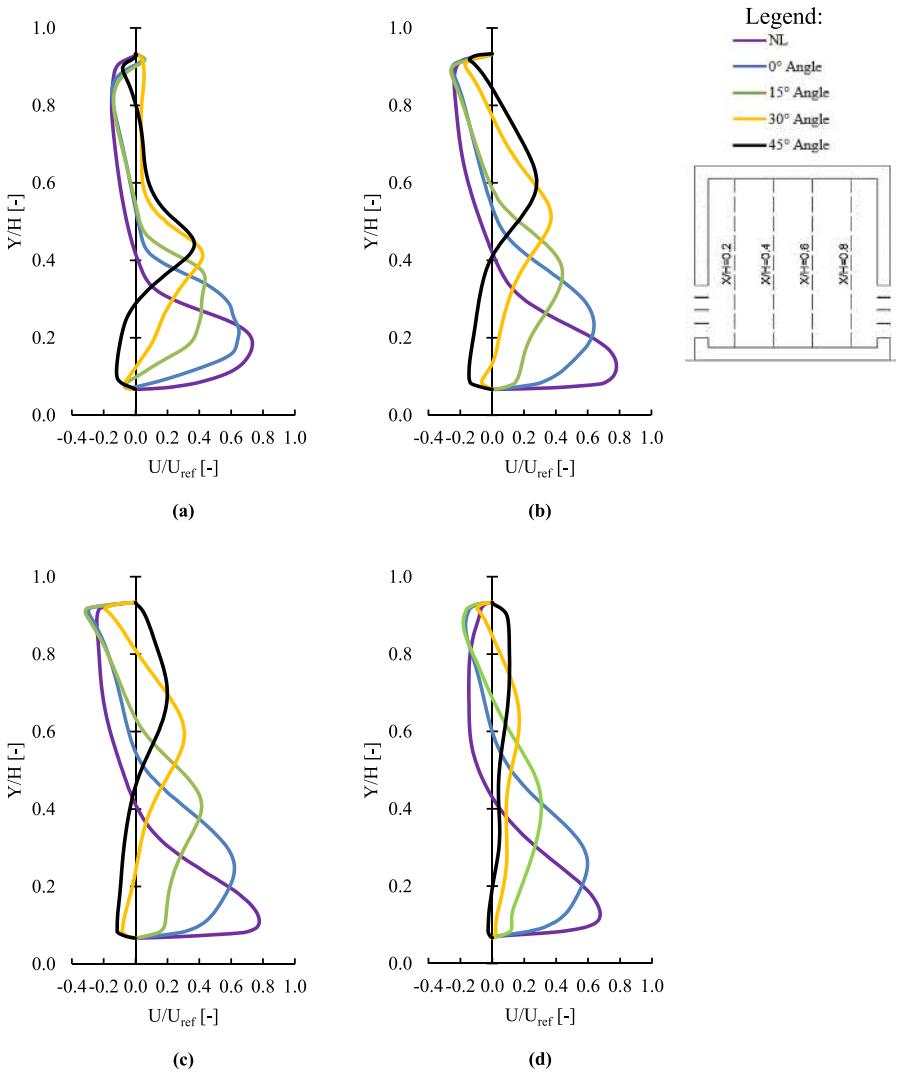

Fig. 10. Y/H against U/U_{ref} for louver angles 0°, 15°, 30° and 45° for bottom-bottom configuration at (a) X/H = 0.2, (b) X/H = 0.4, (c) X/H = 0.6 and (d) X/H = 0.8.

observed when louvers are not present. This is applicable for all opening configurations. Therefore, louvers act as blockages at the opening, thus reducing the k/U_{ref}^2 of the incoming jet as it passes through the building.

4.4. Dimensionless flow rate (DFR)

Equation (12) of DFR can be obtained by dividing the volume flow rate through the building ($\dot{V}$) by the reference velocity, U_{ref} of 1.9 m/s and the opening area, A_o of 0.0028 m^2 (Kosutova et al., 2019; Meroney, 2009). The volume flow rate in the building is obtained from the Fluent console at the windward opening region. DFR is the ratio of the volume flow rate through the opening, and the product of the reference velocity with its opening size.

$$DFR = \frac{\dot{V}}{U_{ref} A_o} \tag{12}$$

Fig. 14 shows top-top configuration achieves the highest DFR for all louver angles of NL, 0°, 15°, 30° and 45° at 0.719, 0.672, 0.593, 0.465 and 0.327 respectively. Such findings of highest volume flow rate obtained by the top-top configuration are in line with results by other authors who have manipulated the opening locations in the presence and absence of louvers (Kosutova et al., 2019; Moey et al., 2021a; Meroney, 2009). The configuration with the second highest DFR at NL configuration is shared between center-center and top-bottom at 0.51. At louver angles of 15°, 30° and 45°, the second highest DFR is obtained by configuration top-bottom.

Center-center louvers at 0° exhibit an interesting characteristic where the reduction in effective opening area, A_E increases the DFR instead of decreasing it. This has also been observed Moey et al. (2021b); where the author's louver configuration at 0° center-center location had a higher DFR than the center-center configuration without louvers and as well as by Zheng et al. (2020).

At louver configuration NL and 0°, the lowest DFR is observed at configuration bottom-top. At configurations with louver angles of 15°, 30° and 45°, the lowest DFR is seen at configuration bottom-bottom.

For the same bottom-bottom configuration, louver angles of 0° and 15° have higher DFR than configuration NL. By observing the U/U_{ref} contours in Table 2 for these configurations, one can observe the jet being directed from the windward bottom toward the leeward opening at the top. The presence of these louvers at the windward bottom increases the building's DFR.

It was predicted that configuration NL would consistently produce the highest DFR across all opening configurations because of the increased unobstructed opening area. This is only true for top-top and top-bottom configurations. Nonetheless, the results show that, for center-center, bottom-bottom and bottom-top, 0° configuration produces a higher DFR than NL configuration.

There is a trend of decreasing DFR as the louver angle increases from

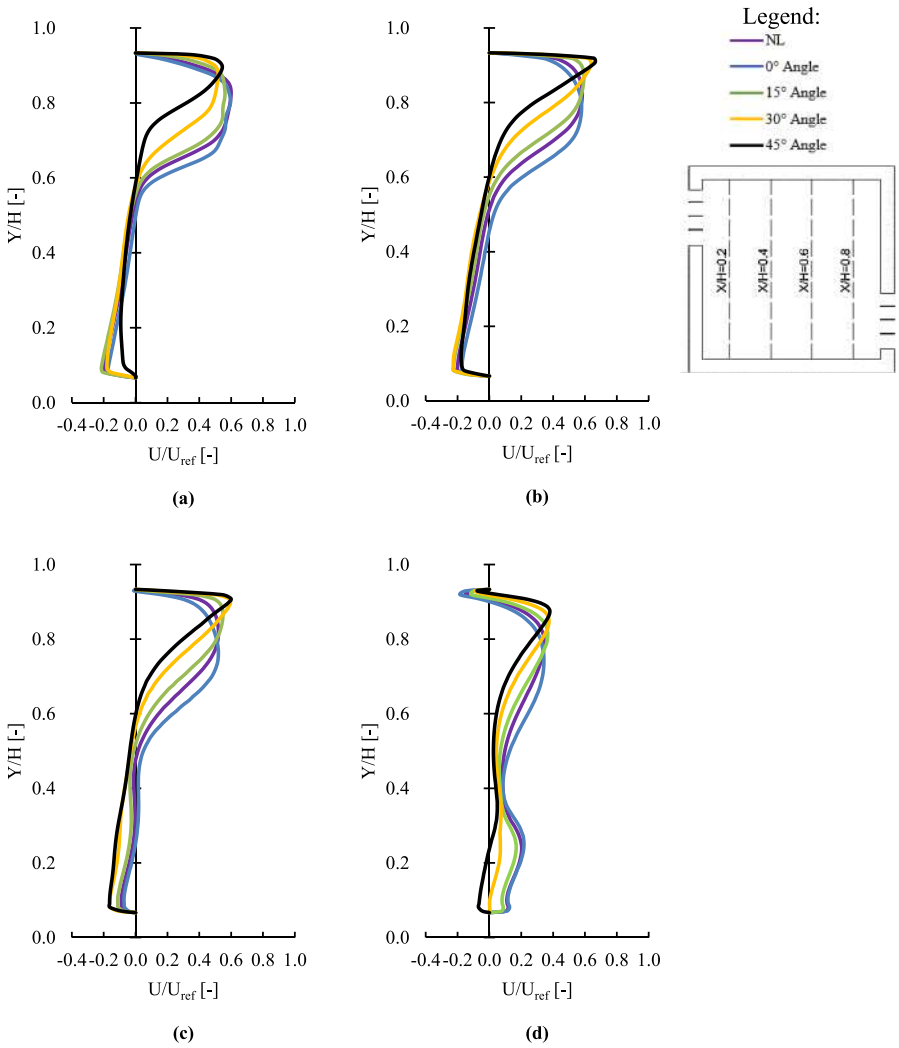

Fig. 11. Y/H against U/U_{ref} for louver angles of 0°, 15°, 30° and 45° for top-bottom configuration at (a) X/H = 0.2, (b) X/H = 0.4, (c) X/H = 0.6 and (d) X/H = 0.8.

0° to 45°. This is attributed to the decrease in effective area, A_E of the opening. The reduction of A_E can arise from a plethora of variables such as the louver geometry, distance between louvers and angle of louvers. In this research, the reduction of A_E arose from the manipulation of the louver angle. This results in a decrease in volume flow rate as the louver angle increases from 0° to 45°. A reduction in the volume flow rate therefore causes a decrease in the DFR. Such findings are similar to that of other authors (Kosutova et al., 2019; Chandrashekaran, 2010; Zheng et al., 2020) who studied the performance of various louver angles with varying A_E.

4.5. Air exchange efficiency (AEE)

When a particular configuration obtains a higher DFR, it is not synonymous with better air mixing within the building. Therefore, the study of air mixing has been performed using Air Exchange Efficiency (ε_A). AEE represents the efficiency of the approaching flow to flush out a ventilated building (Hang and Li, 2011). The AEE is defined by Equation (13) below, where $\overline{\tau}_r$ is the AOA at the leeward opening and τ_{av} is the volume average AOA in the building (van Hooff et al., 2013; Novoselac and Srebric, 2003):

$$\varepsilon_A = \frac{\overline{\tau}_r}{2\tau_{av}} \times 100\ [\%] \tag{13}$$

The AOA was computed by solving the following scalar transport equation (Chanteloup and Mirade, 2009):

$$\frac{\partial}{\partial t}\rho\varphi + \nabla\cdot(\rho U\varphi) - \nabla\cdot(\Gamma\nabla\varphi) = S_\varphi \tag{14}$$

where φ is the scalar to be solved, i.e. AOA, and $S_\varphi = 1$ is the source term. The diffusion coefficient, Γ is calculated using Equation (15) (Chanteloup and Mirade, 2009):

$$\Gamma = \rho D + \frac{\mu_t}{S_{c_t}} \tag{15}$$

where, $D = 2.88 \times 10^{-5}$ m^2/s is the laminar viscosity for air at the operating temperature of 20 ° C, μ_t is the local turbulent viscosity, $S_{c_t} = 0.7$ is the turbulent Schmidt number.

For steady-state conditions, the term $\partial(\rho\varphi)/\partial t$ in Equation (14) is equal to zero. The transport equation was implemented in Fluent as user-defined scalar (UDS) to yield the AOA distribution within the ventilated enclosure. The boundary conditions for the solution of Equation (14) are zero value at the inlet, and zero gradient at walls and outlet surfaces (Gan, 2000).

Table 6 tabulates the contours of the AOA for all configurations whereas Fig. 15 shows the graph for AEE against opening configuration for various louver angles. For all cases, 15° center-center configuration has the highest AEE at 53.4%, indicating that the airflow tends to behave more as a piston-flow (Novoselac and Srebric, 2003). From the U/U$_{ref}$ contour in Table 5, the airflow is directed towards the ceiling with two

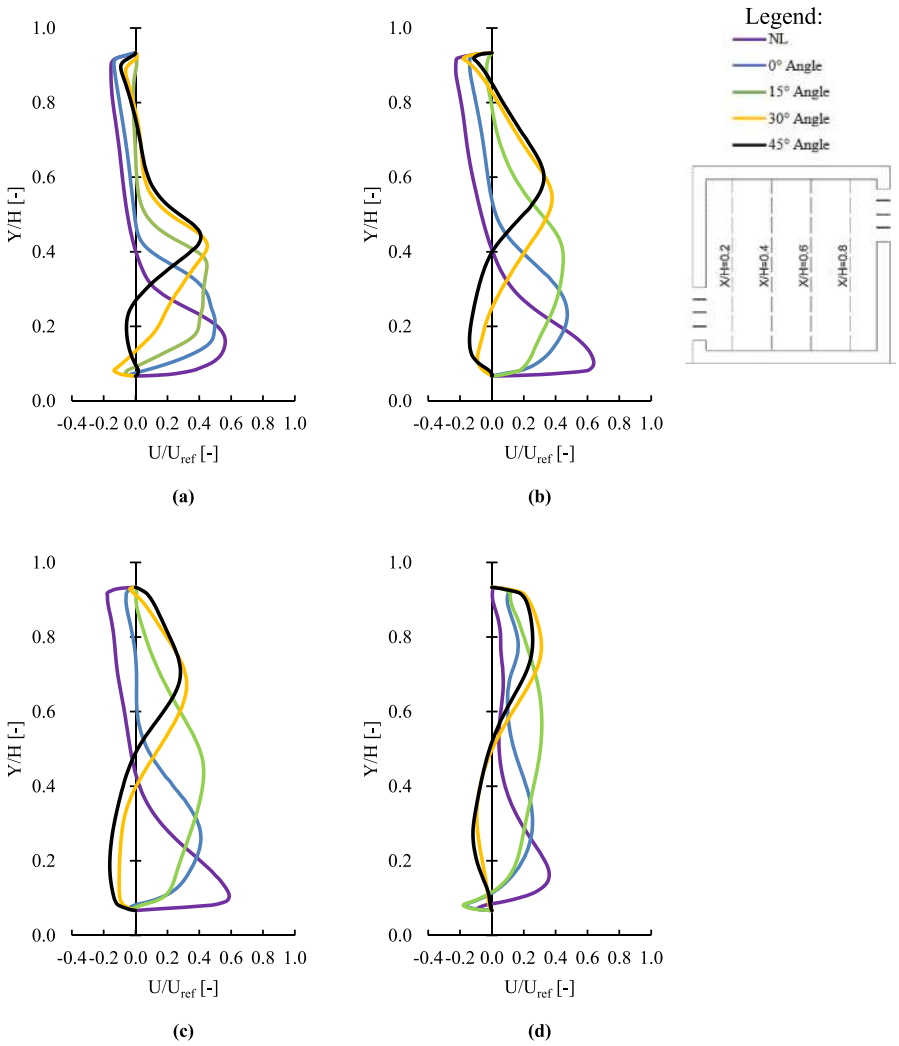

Fig. 12. Y/H against U/U_{ref} for louver angles of 0°, 15°, 30° and 45° for bottom-top configuration at (a) X/H = 0.2, (b) X/H = 0.4, (c) X/H = 0.6 and (d) X/H = 0.8.

circulation zones appear in the top left corner and bottom half of the building that help air mixing inside the building. A closer look at the velocity profiles presented in Fig. 8 reveals that 15° center-center configuration has higher jet velocity with the recirculation zone at the bottom half of the building is less strong than that of 30 ° and 45 ° center-center configurations, in which their respective AEE are 42.9% and 39.7%.

On the contrary, 0° top-top configuration produces the lowest AEE at 20% across all cases. Across all opening positions, top-top configuration consistently produces the lowest AEE despite this configuration having the highest recorded DFR in Fig. 14. This is attributed to the phenomena of a short-circuiting ventilation system. Most of the air resides for a short time, and results in a higher DFR value. However, only a minority of the air flushes the ventilated building, and thus causes a decrease in the AEE values.

Comparing all the configurations with top-top openings, louver angle of 45° produces the highest AEE at 32.1%. By observing the AOA contours, one can notice a larger recirculation region at the middle of the building for top-top 45°. The presence of this recirculation region improves mixing within the building, thus improving its AEE.

For opening configuration top-bottom, louver angle of 0° has the highest AEE at 51.4%. For bottom-top, 15° has the highest AEE at 47% followed by 0° at 43.9%. For top-bottom and bottom-top, 30° and 45° show relatively similar AEE values. It is observed that the effects of high louver angles (30° and 45°) for top-bottom and bottom-top configurations are negligible. The AEE of configuration center-center NL outperformed louver angles of 0°, 30° and 45° (Kosutova et al., 2015) but not 15°. For top-top opening positions, there is an increasing trend of AEE from 15° to 45°.

The presence of 0° louvers at center-center, top-top and bottom-bottom causes short-circuiting of air to occur. However, this phenomenon of short-circuiting of air does not occur for 0° louver angles at top-bottom and bottom-top configurations. On the contrary, the effect of using 0° louvers in top-bottom improves its AEE to 51.4%. Ergo, the usage of 0° louvers to improve the AEE for top-bottom and bottom-top configurations is encouraged.

For bottom-bottom configuration, 30° outperforms NL, 0°, 15° and 45° with an AEE of 50.5%. This is because, the jet is directed to the center of the building with sufficient kinetic energy causing recirculation to occur.

The real-world implications are as such, when louvers are present, higher DFR does not equate to higher AEE. For certain configurations such as bottom-bottom 30°, high AEE is obtained at 50.5% but at the cost of reduced DFR. For mechanical rooms where indoor AHUs are placed, louvers at bottom-bottom configuration are usually installed across each other. Although 30° louvers at bottom-bottom produce higher AEE, its DFR is severely reduced. With that in mind, DFR should be prioritized in this configuration. For naturally cross-ventilated spaces where human comfort is a priority, then AEE should be prioritized instead of DFR.

Table 2
U/U_{ref} contours for varying opening configurations of No-Louvers (NL), 0°, 15°, 30° and 45°.

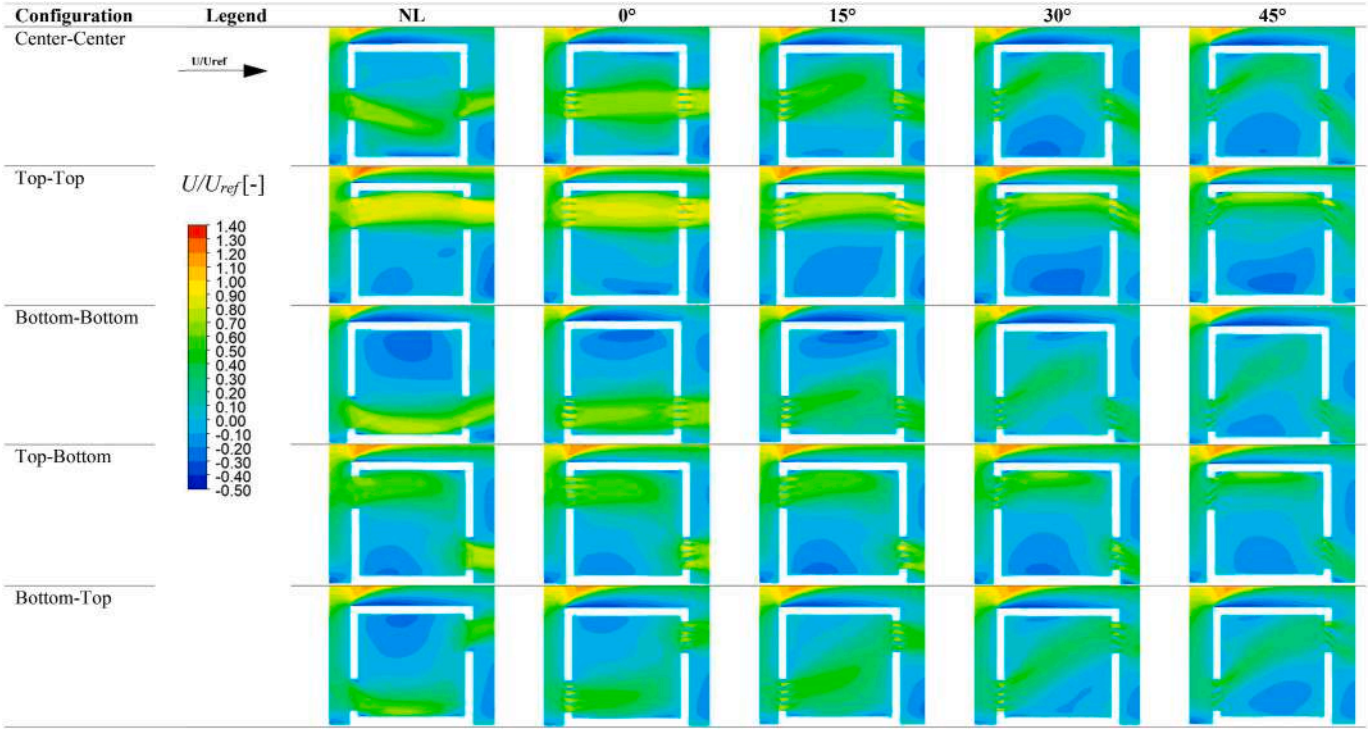

Table 3
Pressure Coefficient, C_p contours for varying opening configurations of No-Louvers (NL), 0°, 15°, 30° and 45°.

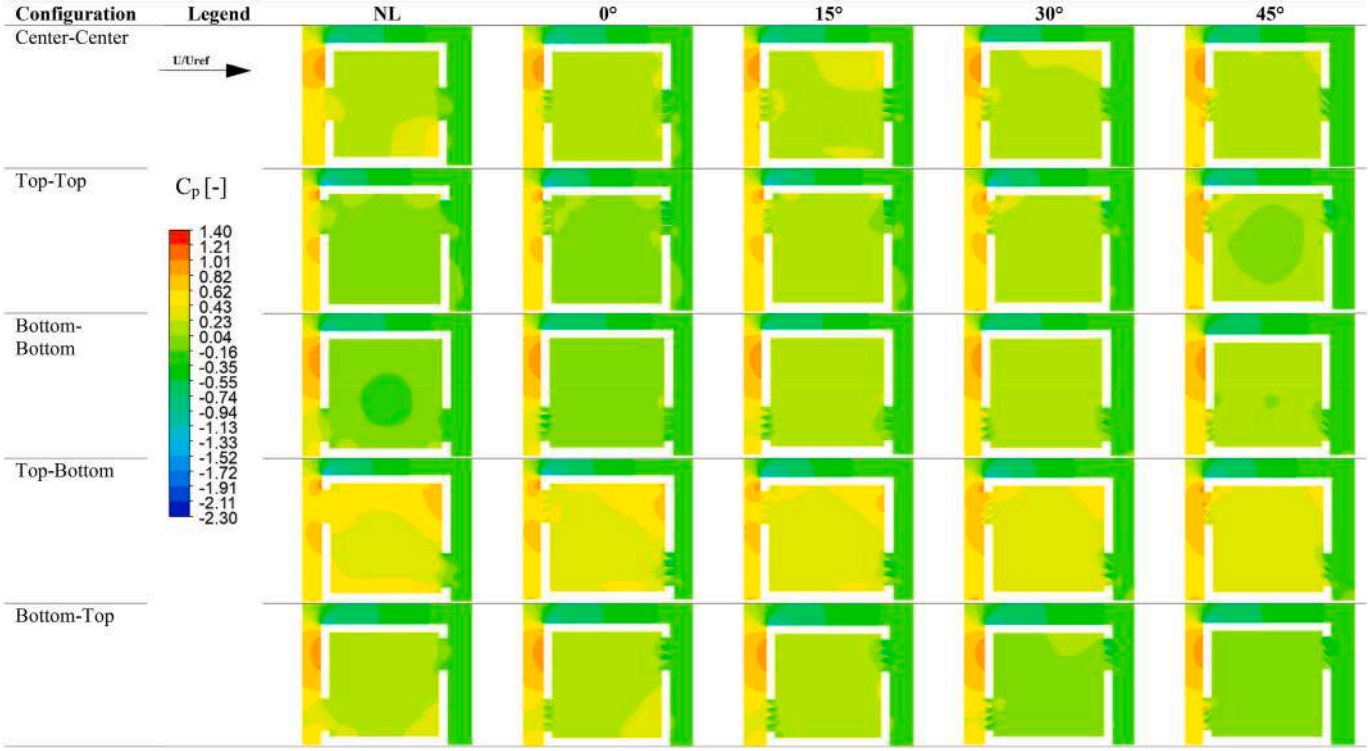

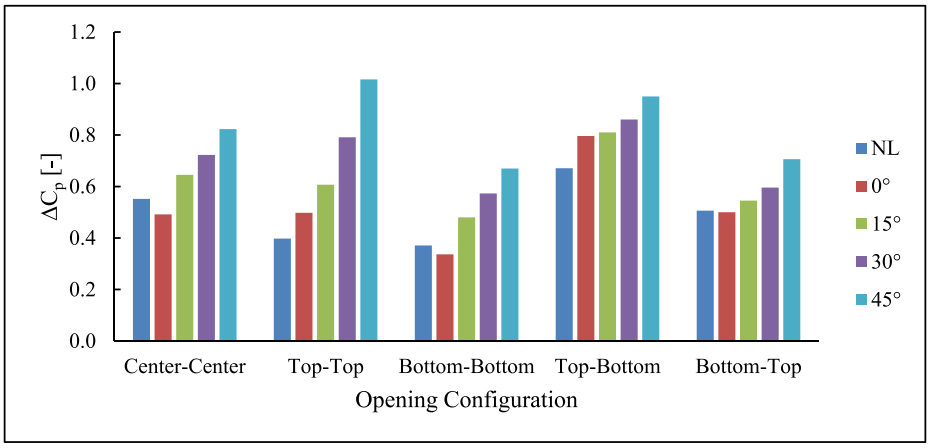

Fig. 13. Change in pressure coefficient between the windward and leeward opening, ΔC_p against opening configurations for various louver angles (°).

Table 4
k/U_{ref}^2 contours for varying opening configurations of No-Louvers (NL), 0°, 15°, 30° and 45°.

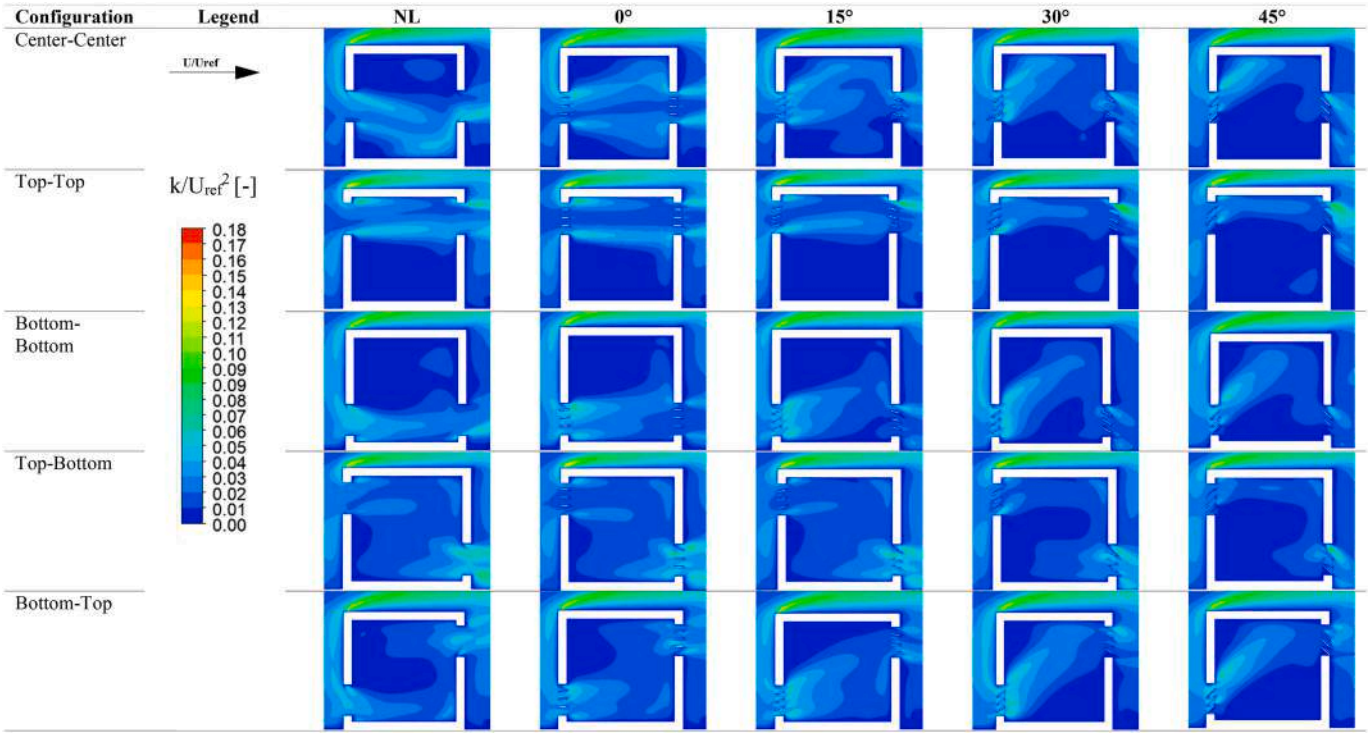

4.6. Relationship between residence time ($\bar{\tau}_r$) and louver angle

It is observed in Fig. 16, residence time increases as the louver angle increases. This increase occurs for all louver angles in all opening configurations. Residence time, $\bar{\tau}_r$ and louver angles experience a sudden increase when transitioning from 30° to 45°.

Bottom-bottom and bottom-top with louver angles of 45° have the highest residence time at 1.73 s. Meanwhile, top-top NL has the lowest residence time at 0.65 s. The residence time can be reduced by improving the DFR that is entering the building. The presence of louvers at the windward reduces the momentum of the approaching jet that enters through the opening, thereby causing increased residence time in the building.

4.7. Factor-optimization (α)

As mentioned previously, there exists a trade-off between AEE and DFR values in the presence of louvers. To quantify this value, the optimal configuration that balances high DFR and high AEE should be obtained. This value can be obtained by factor-optimization, α. The fundamental shortcoming of AEE is, it only provides a quantitative value of how well air is distributed within a room through the flow magnitude and its flow profile. It only measures the building's local mean AOA relative to its volume average AOA. The larger the variance of the local mean AOA compared with its volume average AOA, the lower the AEE; and vice versa.

Consider two buildings of equal size and opening configuration. Building A has a local mean AOA of 25 s, and a volume average AOA of 50 s. Its AEE equals 50%. On the other hand, consider Building B with a

Table 5
U/U_{ref} contours for varying opening configurations of No-Louvers (NL), 0°, 15°, 30° and 45°.

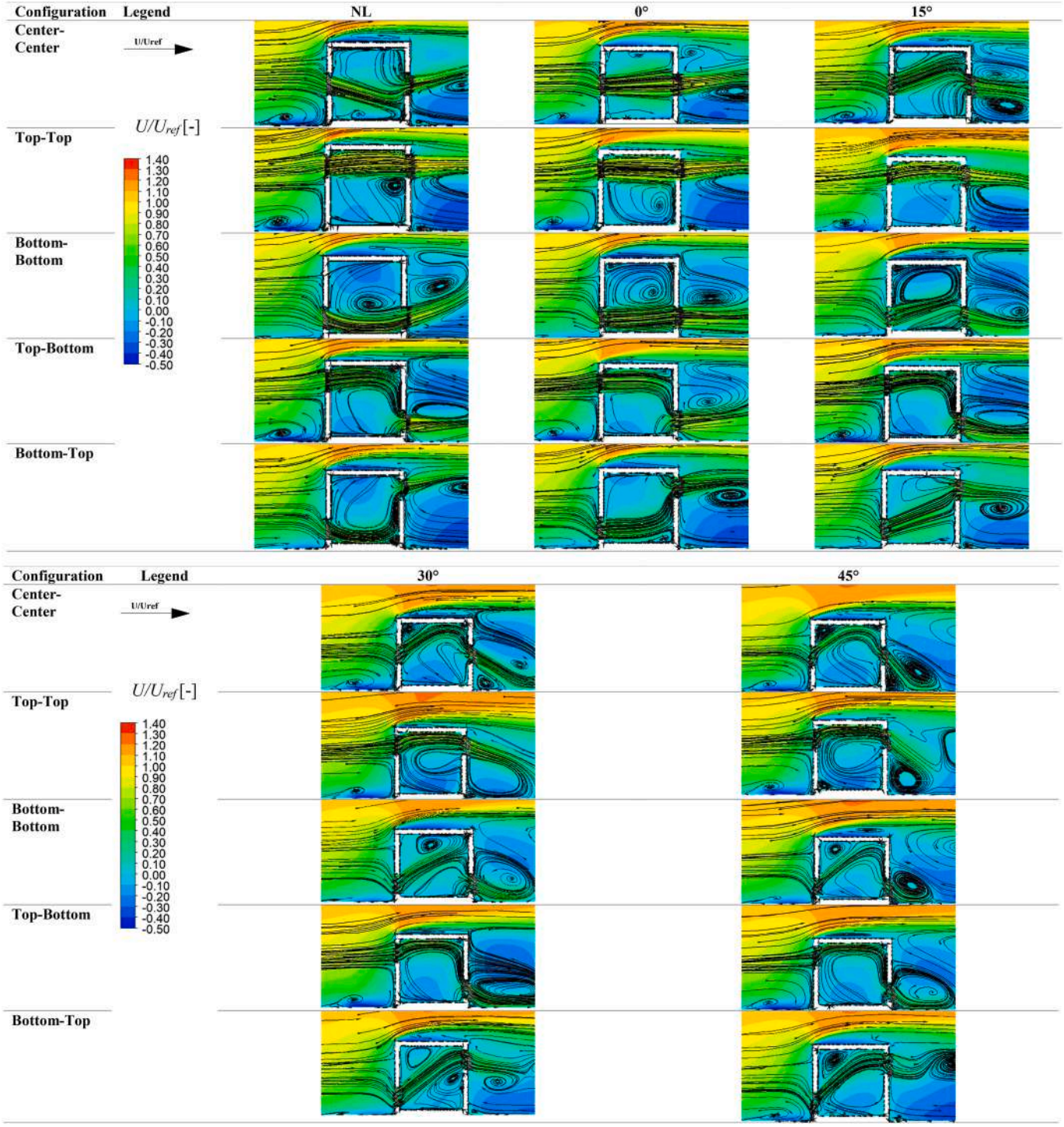

local mean AOA of 1 s, and a volume average AOA of 10 s. Its AEE equals 10%. One might conclude that Building A is preferable to Building B just by observing its AEE values. However, having a local mean AOA of 25 s relative to a local mean AOA of 1 s is 25 times larger.

Having a higher AEE does not equate to a lower local mean AOA within the building. As shown in the previous section, as the louver angle increases, the residence time also increases independent of the opening location. This is because of the reduced DFR through the building. It is also known, as the louver angle increases, its DFR will decrease. Therefore, this predicament can be combatted by using factor-optimization as shown in Equation (16).

$$\alpha = DFR \times \left(\frac{AEE}{100}\right) \tag{16}$$

The optimal configuration that balances DFR and AEE is 0° top-bottom with a factor-optimization value of 0.26 as observed in Fig. 17. Moving on, NL and 15° center-center configuration have the second highest α at 0.25. Therefore, comparing center-center NL and

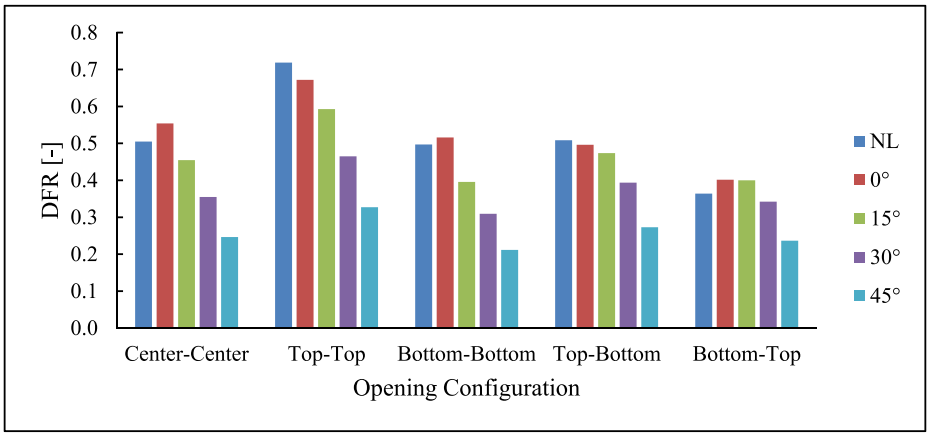

Fig. 14. Dimensionless flow rate (DFR) against louver angle (°) for various opening configurations.

Table 6
Age of Air (AOA) contours for varying opening configurations of No-Louvers (NL), 0°, 15°, 30° and 45°.

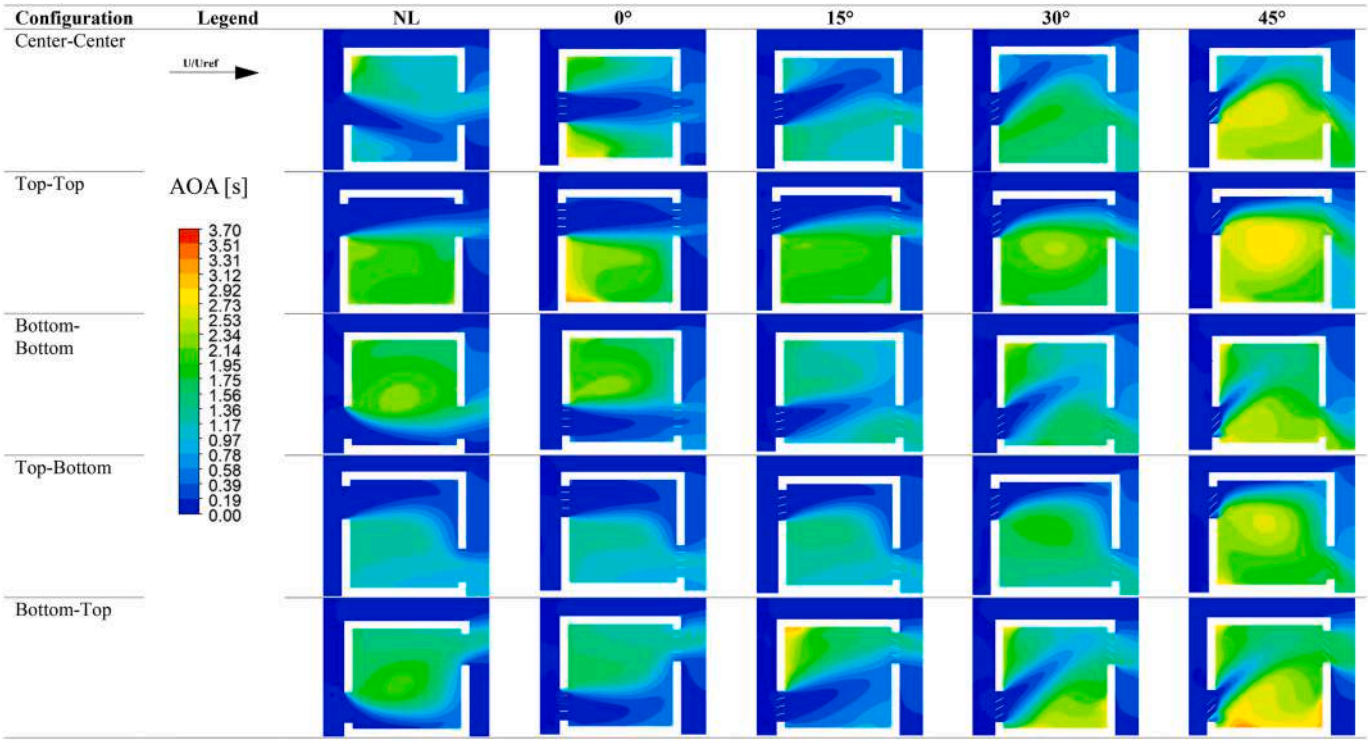

15°, the two configurations provide a relatively equal balance between the two variables of interest.

Moving on, bottom-bottom configuration with 30° louvers has the highest AEE at 50.5% as mentioned previously, meanwhile the 15° louver configuration has an AEE of 44.9%. In retrospect, 30° despite having higher AEE, suffers from a significant decrease in DFR. This reduces its α to 0.16. On the other hand, the 15° louver configuration has a higher value of α at 0.18, thus showing that the 15° louver configuration is the configuration that balances the two variables of DFR and AEE optimally.

Similarly, one can also use factor-optimization to observe that, across all opening configurations, louvers at 45° consistently produce the worst balance between DFR and AEE. The severe reduction in DFR does not provide a notable increase in AEE in any of the opening configurations studied.

5. Conclusions

The effects of varying louver angles and positions have been studied. The opening configurations (i) center-center, (ii) top-top, (iii) bottom-bottom, (iv) top-bottom and (v) bottom-top have been performed with louver configurations of No-Louver (NL), 0°, 15°, 30° and 45°. Where the configurations are defined as 'windward'-'leeward'. The computational domain is designed in accordance with best practices in the literature and numerical simulations are performed by interpreting an Atmospheric Boundary Layer (ABL). The reference grid is selected through grid convergence index (GCI) analysis. The numerical simulation using 3D-RANS equation Renormalization Group (RNG) k-ε with enhanced wall treatment (EWT) shows good agreement via Factor of two of observation (FAC2) analysis. Subsequently, the investigations of the internal air profiles, internal velocities, pressure coefficient, AOA, DFR,

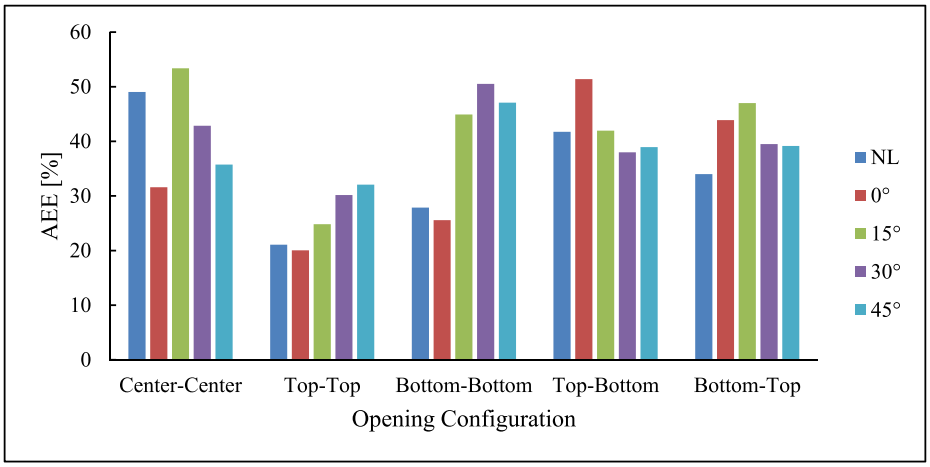

Fig. 15. Air exchange efficiency (AEE) against opening configuration for various louver angles.

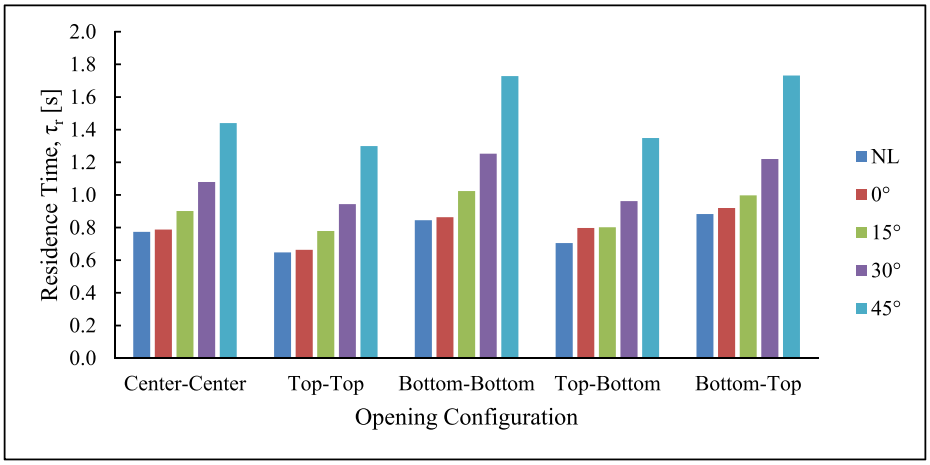

Fig. 16. Residence Time ($\bar{\tau}_r$) [s] against opening configuration for various louver angles.

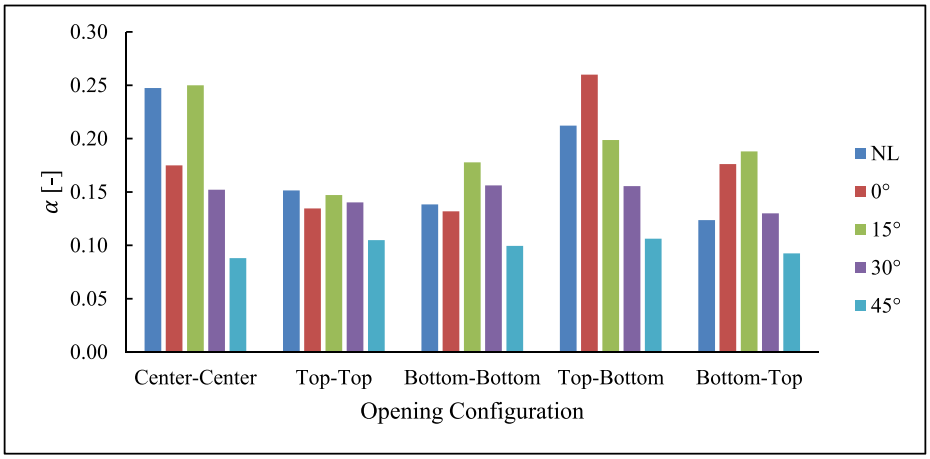

Fig. 17. Factor Optimization (α) against opening configuration for various louver angles.

and AEE have been performed in this paper. This paper has contributed the following advances:

i. The pressure coefficient at the windward opening is dependent on the position of the leeward opening; likewise, the pressure coefficient at the leeward opening is dependent on the position of the windward opening.
ii. There is an increase in the change in pressure coefficient between the windward and leeward opening, ΔC_p as the louver angles increases from 0° to 45° for all opening configurations studied.

iii. Highest DFR is obtained by configuration top-top for all louver configurations of NL, 0°, 15°, 30° and 45°. Such findings are similar to that of existing literature.
iv. Highest AEE is obtained by configuration center-center with 15° louver angles at 53.4% meanwhile top-top configuration with 0° louvers performs the worst at 20%. The former displays good mixing within the building whilst the latter indicate short-circuiting of air.
v. 0° louvers at center-center, top-top and bottom-bottom causes short-circuiting of air. However, this phenomenon of short-circuiting of air does not occur for 0° louver angle at top-bottom and bottom-top configurations. On the contrary, 0° louvers for top-bottom and bottom-top configurations improved their AEE.
vi. Comparing bottom-bottom configurations, 30° louvers obtained the highest AEE at 50.5%. However, this configuration suffers from a severe reduction in DFR. The inability for AEE to account for flow rate has led to the introduction of factor-optimization (α). Through factor-optimization, it is shown that bottom-bottom configuration will balance the variables of DFR and AEE by selecting louvers at 15° instead of 30°.

In conclusion, the study shows thsat opening position alongside louver angle plays an imperative role in its effects on the internal airflow, pressure coefficient, DFR and AEE in natural cross ventilation. Future work should include but are not limited to, the study of velocity profiles at different wind angles, performing studies on various air temperatures, manipulating the thickness of the louver and its surface roughness, changing the wall porosity and finally, studying the performance of complex louver geometries.

CRediT authorship contribution statement

Vin Cent Tai: Conceptualization, Methodology, Software, Validation, Funding acquisition, Resources, Formal analysis. **Joseph Wu Kai-Seun:** Writing – original draft, Investigation, Methodology. **Prasath Reuben Mathew:** Writing – original draft, Investigation, Methodology. **Lip Kean Moey:** Data curation, Investigation, Visualization, Project administration. **Xinwei Cheng:** Formal analysis, Resources, Software. **David Baglee:** Writing – review & editing, Supervision.

Declaration of competing interest

The authors declare the following financial interests/personal relationships which may be considered as potential competing interests:

Vin Cen Tai reports financial support was provided by Malaysia Ministry of Higher Education. Vin Cent Tai reports a relationship with Malaysia Ministry of Higher Education that includes: funding grants.

Data availability

Data will be made available on request.

Acknowledgment

The project is funded by the Ministry of Education Malaysia, under the Fundamental Research Grant Scheme (FRGS). Grant No: FRGS/1/2017/TK07/SEGI/02/1.

References

Aflaki, A., Mahyuddin, N., Mahmoud Awad, Z.A.C., Baharum, M.R., 2014. Relevant indoor ventilation by windows and apertures in tropical climate: a review study. E3S Web. Conf. 3 https://doi.org/10.1051/e3sconf/20140301025.

Chandrashekaran, D., 2010. Air Flow through Louvered Openings: Effect of Louver Slats on Air Movement inside a Space. Accessed: Feb. 05, 2021. [Online]. Available: http://digitallibrary.usc.edu/cdm/ref/collection/p15799coll127/id/388014.

Chanteloup, V., Mirade, P.S., 2009. Computational fluid dynamics (CFD) modelling of local mean age of air distribution in forced-ventilation food plants. J. Food Eng. 90 (1), 90–103. https://doi.org/10.1016/j.jfoodeng.2008.06.014.

El Gharbi, N., Absi, R., Benzaoui, A., Amara, E.H., 2009. Effect of near-wall treatments on airflow simulations. In: International Conference on Computational Methods for Energy Engineering and Environment. ICCM3E, pp. 185–189 [Online]. Available: http://arxiv.org/abs/1011.6043.

Elwan, M., Rizk, A., El-Morsi, M., 2018. A review on wind - driven cross - ventilation techniques inside single rooms. Int. J. Sci. Eng. Res. 6 (October), 75–93.

Gan, G., 2000. Effective depth of fresh air distribution in rooms with single-sided natural ventilation. Energy Build. 31 (1), 65–73. https://doi.org/10.1016/S0378-7788(99)00006-7.

Gilani, S., Montazeri, H., Blocken, B., 2013. CFD simulation of temperature stratification for a building space: validation and sensitivity analysis. In: 13th Conference of the International Building Performance Simulation Association, pp. 504–511.

Green Building Council, U.S., 2000. Optimize Energy Performance - LEED 2.0 - HVAC. U. S. Green Building Council. https://www.usgbc.org/credits/commercial-interiors/v20/eac13. (Accessed February 2021), 03.

Hang, J., Li, Y., 2011. Age of air and air exchange efficiency in high-rise urban areas and its link to pollutant dilution. Atmos. Environ. 45 (31), 5572–5585. https://doi.org/10.1016/j.atmosenv.2011.04.051.

Hassan, J.S., Zin, R.M., Majid, M.Z.A., Balubaid, S., Hainin, M.R., 2014. Building energy consumption in Malaysia: an overview. J. Teknol. 70 (7), 33–38. https://doi.org/10.11113/jt.v70.3574.

Kosutova, K., van Hooff, T., Blocken, B., Hensen, J., 2015. CFD analysis of ventilative cooling in a generic isolated building equipped with ventilation Louvers. In: Healthy Buildings Europe, vol. 2015 (May).

Kosutova, K., van Hooff, T., Vanderwel, C., Blocken, B., Hensen, J., 2019. Cross-ventilation in a generic isolated building equipped with louvers: wind-tunnel experiments and CFD simulations. Build. Environ. 154, 263–280. https://doi.org/10.1016/j.buildenv.2019.03.019. March.

Kouhirostami, M., 2020. Impact of Louvers Geometry of Window on Cross-Ventilation in a Generic Isolated Building in Rigid Climate. Case Study, Lubbok, TX.

Krishna, Z., et al., 2019. Ansys mosaic poly-hexcore mesh for high-lift aircraft configuration. 21 st Annu. CFD Symp. (September), 1–11.

Meroney, R.N., 2009. CFD prediction of airflow in buildings for natural ventilation. In: 11th Americas Conference on Wind Engineering, pp. 1–11.

Moey, L.K., Adam, N.M., Ahmad, K.A., Abdullah, L.C., 2018. Wind tunnel study of different roof geometry configurations for wind induced natural ventilation into stairwell in tropical climate. Int. J. Eng. Res. 13 (5), 2635–2647.

Moey, L.K., Chan, K.L., Tai, V.C., Go, T.F., Chong, P.L., 2021a. Investigation on the effect of opening position across an isolated building for wind- driven cross ventilation. J. Mech. Eng. Sci. 15 (2), 8141–8152. https://doi.org/10.15282/jmes.15.2.2021.14.0639.

Moey, L.K., Alyazidi, S.M.S., Tai, V.C., Kai-Seun, J.W., Mathew, P.R., 2021b. Studying opening ratios in the presence and absence of louvers in cross ventilation using CFD. In: International Conference on Mechanical Engineering Research, pp. 1–16.

Novoselac, A., Srebric, J., 2003. Comparison of air exchange efficiency and contaminant removal effectiveness as IAQ indices. Build. Eng. 109 (4663), 339–349. PART 2.

Perén, J.I., van Hooff, T., Leite, B.C.C., Blocken, B., 2015. CFD analysis of cross-ventilation of a generic isolated building with asymmetric opening positions: impact of roof angle and opening location. Build. Environ. 85, 263–276. https://doi.org/10.1016/j.buildenv.2014.12.007.

Ramponi, R., Blocken, B., 2012. CFD simulation of cross-ventilation for a generic isolated building: impact of computational parameters. Build. Environ. 53, 34–48. https://doi.org/10.1016/j.buildenv.2012.01.004.

Schatzmann, M., Olesen, H., Franke, J., 2010. Cost 732 Model Evaluation Case Studies : Approach and Results, vol. 732. COST Action, p. 732.

Shaikh, P.H., Nor, N.B.M., Sahito, A.A., Nallagownden, P., Elamvazuthi, I., Shaikh, M.S., 2017. Building energy for sustainable development in Malaysia: a review. Renew. Sustain. Energy Rev. 75 https://doi.org/10.1016/j.rser.2016.11.128. May 2015.

Shirzadi, M., Mirzaei, P.A., Tominaga, Y., 2020. CFD analysis of cross-ventilation flow in a group of generic buildings: comparison between steady RANS, LES and wind tunnel experiments. Build. Simulat. 13 (6), 1353–1372. https://doi.org/10.1007/s12273-020-0657-7.

Shirzadi, M., Mirzaei, P.A., Tominaga, Y., 2021. LES analysis of turbulent fluctuation in cross-ventilation flow in highly-dense urban areas. J. Wind Eng. Ind. Aerod. 209 https://doi.org/10.1016/j.jweia.2020.104494. January.

Sofotasiou, P., Hughes, B., Ghani, S.A., 2017. CFD optimisation of a stadium roof geometry: a qualitative study to improve the wind microenvironment. Sustain. Build 2, 8. https://doi.org/10.1051/sbuild/2017006. January.

Tominaga, Y., Blocken, B., 2016. Wind tunnel analysis of flow and dispersion in cross-ventilated isolated buildings: impact of opening positions. J. Wind Eng. Ind. Aerod. 155, 74–88. https://doi.org/10.1016/j.jweia.2016.05.007.

United States of America Department of Energy, 2015. An Assessment of Energy Technologies and Research Opportunities.

van Hooff, T., Blocken, B., 2010. Coupled urban wind flow and indoor natural ventilation modelling on a high-resolution grid: a case study for the Amsterdam ArenA stadium. Environ. Model. Software 25 (1), 51–65. https://doi.org/10.1016/j.envsoft.2009.07.008.

van Hooff, T., Blocken, B., van Heijst, G.J.F., 2013. On the suitability of steady RANS CFD for forced mixing ventilation at transitional slot Reynolds numbers. Indoor Air 23 (3), 236–249. https://doi.org/10.1111/ina.12010.

van Hooff, T., Blocken, B., Tominaga, Y., 2017. On the accuracy of CFD simulations of cross-ventilation flows for a generic isolated building: comparison of RANS, LES and

experiments. Build. Environ. 114, 148–165. https://doi.org/10.1016/j.buildenv.2016.12.019.
Wilcox, D.C., 2006. Turbulence Modeling for CFD, third ed. DCW Industries Inc., La Cañada, California.
Zheng, J., Tao, Q., Li, L., 2020. Numerical study of wind environment of a low-rise building with shading louvers: sensitive analysis and evaluation of cross ventilation. J. Asian Architect. Build Eng. 19 (6), 541–558. https://doi.org/10.1080/13467581.2020.1758113.